ON THE COMPOSITION OF YOUNG,
DIRECTLY IMAGED GIANT PLANETS

ON THE COMPOSITION OF YOUNG, DIRECTLY IMAGED GIANT PLANETS

J. I. MOSES[1], M. S. MARLEY[2], K. ZAHNLE[2], M. R. LINE[3], J. J. FORTNEY[3], T. S. BARMAN[4],
C. VISSCHER[1,5], N. K. LEWIS[6], AND M. J. WOLFF[1]

[1] Space Science Institute, 4750 Walnut Street, Suite 205, Boulder, CO 80301, USA; jmoses@spacescience.org
[2] NASA Ames Research Center, Moffett Field, CA 94035, USA
[3] Department of Astronomy and Astrophysics, University of California, Santa Cruz, CA 95064, USA
[4] Lunar and Planetary Laboratory, University of Arizona, Tucson, AZ 85721, USA
[5] Dordt College, Sioux Center, IA 51250, USA
[6] Space Telescope Science Institute, Baltimore, MD 21218, USA

ABSTRACT

The past decade has seen significant progress on the direct detection and characterization of young, self-luminous giant planets at wide orbital separations from their host stars. Some of these planets show evidence for disequilibrium processes like transport-induced quenching in their atmospheres; photochemistry may also be important, despite the large orbital distances. These disequilibrium chemical processes can alter the expected composition, spectral behavior, thermal structure, and cooling history of the planets, and can potentially confuse determinations of bulk elemental ratios, which provide important insights into planet-formation mechanisms. Using a thermo/photochemical kinetics and transport model, we investigate the extent to which disequilibrium chemistry affects the composition and spectra of directly imaged giant exoplanets. Results for specific "young Jupiters" such as HR 8799 b and 51 Eri b are presented, as are general trends as a function of planetary effective temperature, surface gravity, incident ultraviolet flux, and strength of deep atmospheric convection. We find that quenching is very important on young Jupiters, leading to CO/CH_4 and N_2/NH_3 ratios much greater than, and H_2O mixing ratios a factor of a few less than, chemical-equilibrium predictions. Photochemistry can also be important on such planets, with CO_2 and HCN being key photochemical products. Carbon dioxide becomes a major constituent when stratospheric temperatures are low and recycling of water via the $H_2 + OH$ reaction becomes kinetically stifled. Young Jupiters with effective temperatures $\lesssim 700$ K are in a particularly interesting photochemical regime that differs from both transiting hot Jupiters and our own solar-system giant planets.

Key words: planetary systems – planets and satellites: atmospheres – planets and satellites: composition – planets and satellites: gaseous planets – planets and satellites: individual (51 Eri b, HR 8799 b)

Supporting material: tar.gz file

1. INTRODUCTION

Most of the exoplanets discovered to date have been identified through transit observations or radial-velocity measurements—techniques that favor the detection of large planets orbiting close to their host stars. Direct detection of a planet within the overwhelmingly glare and non-negligible point-spread function of its brighter star is challenging and requires high-contrast observations, often with adaptive-optics techniques from large telescopes on the ground or in space. As a result of these observational challenges, direct imaging favors the detection of massive, self-luminous (i.e., young) giant planets at wide orbital separations from their host stars. These "young Jupiters" are hot at depth because the leftover accretional and gravitational potential energy from the planet's formation has not had time to convect up through the atmosphere and be radiated away yet. Only ∼3% of the currently confirmed exoplanets[7] have been detected through direct imaging, but these planetary systems have high intrinsic interest. For example, they serve as potential analogs to our own solar system in its formative years, when Jupiter and our other giant planets were born and evolved behind ice condensation fronts in the solar nebula but never migrated

inward—unlike, apparently, many of the known close-in, transiting, extrasolar giant planets. Directly imaged planets therefore provide a window into our own past and provide important clues to our solar system's origin and evolution (see, e.g., Madhusudhan et al. 2014). Wavelength-dependent photometry or spectra of directly imaged planets can also provide useful constraints on atmospheric properties such as composition, thermal structure, metallicity, bulk elemental ratios, and the presence or absence of clouds (see the reviews of Bailey 2014; Madhusudhan et al. 2014, 2016; Crossfield 2015).

Short-period, transiting "hot Jupiters" and directly imaged "young Jupiters" both have similar effective temperatures, often ranging from ∼500 to 2500 K. However, in terms of their thermal structure and spectral appearance, directly imaged planets have more in common with brown dwarfs than with hot Jupiters (e.g., Burrows et al. 2003; Fortney et al. 2008b; Bowler 2016). In particular, the stratospheres (radiative regions) of directly imaged planets and brown dwarfs are much cooler than those of highly irradiated hot Jupiters, and the cooler regions overlying hot continuum regions at depth can result in potentially deeper molecular absorption bands being present in emission spectra (Madhusudhan et al. 2014). It can therefore be easier to detect atmospheric molecules on young Jupiters and brown dwarfs, unless high clouds are present to obscure the absorption features.

---

[7] See http://exoplanet.eu, http://exoplanetarchive.ipac.caltech.edu, or http://www.openexoplanetcatalogue.com.

One drawback of direct imaging is that the planet's radius and mass cannot be well determined, unlike the situation with, respectively, transit observations and radial-velocity measurements. Instead, the mass and radius of directly imaged planets are more loosely constrained through atmospheric modeling and comparisons with the observed luminosity and spectral/photometric behavior, often in combination with estimates of the age of the system and constraints from evolutionary models. The theoretical modeling and model-data comparisons can result in degeneracies between the planet's apparent size, surface gravity, effective temperature, and cloud properties (e.g., Marley et al. 2007, 2012; Barman et al. 2011a, 2011b, 2015; Currie et al. 2011; Madhusudhan et al. 2011; Spiegel & Burrows 2012; Bonnefoy et al. 2013, 2016; Lee et al. 2013; Skemer et al. 2014; Baudino et al. 2015; Morzinski et al. 2015; Zurlo et al. 2016).

On the other hand, the identification of molecular features in the observed spectra is typically unambiguous on young Jupiters (e.g., Konopacky et al. 2013; Barman et al. 2015), and H_2O, CO, and/or CH_4 have been detected in in spectra from several directly imaged planets (Patience et al. 2010; Barman et al. 2011a, 2011b, 2015; Janson et al. 2013; Konopacky et al. 2013; Oppenheimer et al. 2013; Snellen et al. 2014; Chilcote et al. 2015; Macintosh et al. 2015). The apparent deficiency of methane features on many cooler directly imaged planets, in conflict with chemical equilibrium expectations, has been argued as evidence for disequilibrium processes like transport-induced quenching on these planets (e.g., Bowler et al. 2010; Hinz et al. 2010; Janson et al. 2010, 2013; Barman et al. 2011a, 2011b, 2015; Galicher et al. 2011; Marley et al. 2012; Skemer et al. 2012, 2014; Currie et al. 2014; Ingraham et al. 2014; Zahnle & Marley 2014), and so many of the above groups included quenching in their theoretical modeling (see Visscher & Moses 2011; Zahnle & Marley 2014 for more details about CO $\leftrightarrow$ CH_4 quenching on directly imaged planets and brown dwarfs). Other disequilibrium chemical processes such as photochemistry have been assumed to be unimportant due to the large orbital distances of these planets (Crossfield 2015); however, the young stellar hosts of directly imaged planets tend to be bright in the ultraviolet, making photochemistry potentially important (e.g., Zahnle et al. 2016).

The goal of the present investigation is to quantify the extent to which disequilibrium chemical processes like photochemistry and quenching affect the composition and spectra of young, directly imaged planets. Our main theoretical tool is a thermochemical-photochemical kinetics and transport model (e.g., Moses et al. 2011, 2013a, 2013b; Visscher & Moses 2011) that tracks the chemical production, loss, and transport of the most abundant gas-phase species in a hydrogen-dominated planetary atmosphere. We calculate the expected composition of specific directly imaged exoplanets such as 51 Eri b and HR 8799 b, for which observational spectra are available, as well as investigate how the composition of generic "young Jupiters" is affected by planetary parameters such as the effective temperature, surface gravity, incident ultraviolet flux, and the strength of atmospheric mixing. We also explore how disequilibrium chemistry affects the resulting spectra of directly imaged planets.

2. THEORETICAL MODEL

To calculate the vertical profiles of atmospheric species on directly imaged planets, we use the Caltech/JPL KINETICS code (Allen et al. 1981; Yung et al. 1984) to solve the coupled one-dimensional (1D) continuity equations for 92 neutral carbon-, oxygen-, nitrogen-, and hydrogen-bearing species that interact through ~1650 kinetic reactions. Hydrocarbons with up to six carbon atoms are considered, although the reaction list becomes increasingly incomplete the heavier the molecule. We do not consider ion chemistry from photoionization (Lavvas et al. 2014) or galactic-cosmic-ray ionization (Rimmer et al. 2014). Ion chemistry is not expected to affect the mixing ratios of the dominant gas species, but it will likely augment the production of heavy organic molecules, just as on Titan (e.g., Vuitton et al. 2007; Waite et al. 2007). Lacking any definitive evidence to the contrary for directly imaged giant planets, we assume the atmospheres have a solar elemental composition.

The reaction list includes both "forward" (typically exothermic) reactions and their reverses, where the reverse reaction rate coefficient is calculated from the forward rate coefficient and equilibrium constant assuming thermodynamic reversibility (e.g., Visscher & Moses 2011; Heng et al. 2016). All reactions except those involving photolysis are reversed. The fully reversed reaction mechanism ensures that thermochemical equilibrium is maintained kinetically in the hotter deep atmosphere, while disequilibrium photochemistry and transport processes can take over and dominate in the cooler upper atmosphere (e.g., Line et al. 2011; Moses et al. 2011; Kopparapu et al. 2012; Miller-Ricci Kempton et al. 2012; Venot et al. 2012; Agúndez et al. 2014a; Hu & Seager 2014; Miguel & Kaltenegger 2014; Benneke 2015; Zahnle et al. 2016). The model automatically accounts for the transport-induced quenching of species, whereby mixing ratios are "frozen in" at a constant mixing ratio above some quench pressure as vertical transport processes start to dominate over the chemical reactions that are attempting to drive the atmosphere back toward thermochemical equilibrium (Prinn & Barshay 1977; Lewis & Fegley 1984; Fegley & Lodders 1994).

The quenching process depends on the adopted reaction mechanism (cf. Visscher et al. 2010b; Line et al. 2011; Moses et al. 2011; Visscher & Moses 2011; Venot et al. 2012; Moses 2014; Zahnle & Marley 2014; Wang et al. 2015; Rimmer & Helling 2016). Our chemical reaction list is taken from Moses et al. (2013a) and includes a thorough review of the key reaction mechanisms of potential importance in the quenching of CO $\leftrightarrows$ CH_4 and N_2 $\leftrightarrows$ NH_3 (Moses et al. 2010, 2011, 2013a, 2013b; Visscher et al. 2010b; Visscher & Moses 2011; Moses 2014); further details of the thermo/photochemical kinetics and transport model are provided in the above papers, and the reaction list is available as supporting material. Note that we do not include the fast rate coefficient for $H + CH_3OH \rightarrow CH_3 + H_2O$ suggested by Hidaka et al. (1989) that is controlling CO–CH_4 quenching in the Venot et al. (2012) mechanism. As discussed by Norton & Dryer (1990), Lendvay et al. (1997), and Moses et al. (2011), this reaction actually possesses a very high energy barrier (>10,000 K) and is not expected to be important under either methanol-combustion conditions or in the deep atmospheres of hydrogen-rich exoplanets—in other words, the Hidaka et al. rate coefficient greatly overestimates the rate of this reaction.

Zahnle & Marley (2014) adopt the upper limit for this reaction as suggested by Norton & Dryer (1989) and find it to be important but not typically dominant in CO–CH$_4$ quenching, except for cooler brown dwarfs with weak mixing. We adopt the much smaller rate coefficient as calculated by Moses et al. (2011), and this reaction does not play a role in CO–CH$_4$ quenching. Similarly, we do not adopt the relatively fast rate-coefficient expression for NH$_2$ + NH$_3$ → N$_2$H$_3$ + H$_2$ estimated by Konnov & De Ruyck (2000) that is affecting N$_2$-NH$_3$ quenching in the Venot et al. (2012) mechanism, as again, this reaction is expected to have a high-energy barrier and be slower under relevant conditions than the Konnov and De Ruyck estimate (e.g., Dean et al. 1984).

Our model grids consist of 198 vertical levels separated uniformly in log(pressure) (providing multiple grid levels per scale height to insure accurate diffusion calculations), with a bottom level defined where the deep atmospheric temperature on an adiabatic gradient is greater than ~2700 K (to insure that the N$_2$-NH$_3$ quench point is captured), and a top level residing at ~10^{-8} mbar (to insure all the molecular absorbers are optically thin in the ultraviolet). The top region of our model grid extends through what would typically be the "thermosphere" of the planet; however, we neglect non-stellar sources of thermospheric heating (such as auroral and Joule heating), which are poorly understood but are important on our solar-system giant planets (e.g., Yelle & Miller 2004; Nagy et al. 2009). Our results should therefore only be considered reliable from the deep troposphere on up to the homopause level at the base of the thermosphere (near 10^{-4} to 10^{-6} mbar, depending on the strength of atmospheric mixing), where molecular diffusion acts to limit the abundance of heavy molecular and atomic species in the lighter background hydrogen atmosphere.

The thermal structure itself is not calculated self-consistently but is adopted from two different atmospheric models: (1) the radiative-convective equilibrium models described in McKay et al. (1989), Marley et al. (1999, 2002), and Saumon & Marley (2008), with updates as described in Marley et al. (2012), and (2) the PHOENIX-based models described in Hauschildt et al. (1997), Allard et al. (2001), and Barman et al. (2011a), with updates as described in Barman et al. (2015). We add a smoothly varying, nearly isothermal profile at the top of the above-mentioned theoretical model profiles to extend our grids to lower pressures, except in isolated cases where we test the effects of a hotter (1000 K) thermosphere. Figure 1 shows the temperature profiles adopted for our cloud-free generic directly imaged planets, as a function of effective temperature T_{eff} for two different assumed 1-bar surface gravities, log(g) = 3.5 and 4.0 cgs. These profiles are calculated without considering stellar irradiation—for all directly imaged planets discovered to date, the external radiation field has little effect on the thermal profile due to the planets' large orbital distance and strong internal heat flux. As such, the internal heat completely dominates the thermal structure, and temperatures on these planets are hotter at depth and colder in the stratospheric radiative region than for close-in transiting giant planets of the same effective temperature. The profiles from Figure 1 were generated with the NASA Ames brown-dwarf and exoplanet structure models (e.g., Marley et al. 2012); tables with the individual pressure–temperature structure from these models are available as supporting material. Disequilibrium processes like photochemistry and quenching are expected to have a
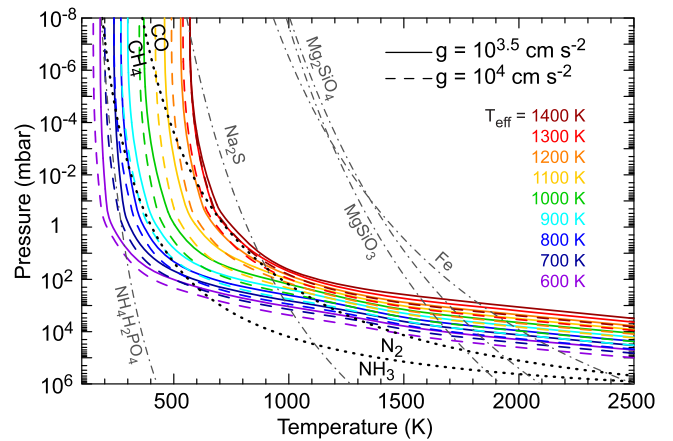

Figure 1. Theoretical temperature profiles for generic directly imaged planets from the radiative-convective equilibrium model of Marley et al. (2012), as a function of effective temperature T_{eff} for an assumed surface gravity (in cm s^{-2}) of log(g) = 3.5 (colored solid lines) and log(g) = 4.0 (colored dashed lines) and assumed solar composition atmosphere in chemical equilibrium. Profiles are shown every 100 K from T_{eff} = 600 to 1400 K. The gray dot-dashed lines show the condensation curves for some important atmospheric cloud-forming species (as labeled) for an assumed solar-composition atmosphere. The thicker dotted black lines represent the boundaries where CH$_4$ and CO have equal abundances and where N$_2$ and NH$_3$ have equal abundance in chemical equilibrium for solar-composition models. Methane and ammonia dominate to the lower left of these curves, while CO and N$_2$ dominate to the upper right. Note that all the profiles remain within the CO-dominated regime at depth, whereas all except for the hottest planets transition to the CH$_4$-dominated regime at higher altitudes.

relatively minor effect on the thermal structure (e.g., Agúndez et al. 2014b), unless these processes affect the H$_2$O abundance.

Given a temperature-pressure profile, the NASA CEA code of Gordon & McBride (1994) is then used to determine the chemical-equilibrium abundances, which are used as initial conditions in the photochemical model. We use the protosolar abundances listed in Table 10 of Lodders (2010) to define our "solar" composition. The mean molecular mass profile from the chemical-equilibrium solution, the pressure–temperature profile, and the assumed physical parameters of the planet become inputs to the hydrostatic equilibrium equation, whose solution sets the altitude scale and other atmospheric parameters along the vertical model grid. For a surface (1-bar) gravity of $g = 10^4$ cm s^{-2}, the planet mass M_p is $4M_J$, and for $g = 10^{3.5}$ cm s^{-2}, $M_p = 2M_J$. For boundary conditions, we assume the fluxes of the species are zero at the top and bottom of the model. The models are run until steady state, with a convergence criterion of 1 part in 1000. For the photochemical calculations, the atmospheric extinction is calculated from the absorption and multiple Rayleigh scattering of gases only—aerosol extinction is ignored due to a lack of current predictive capability regarding the hazes. The atmospheric radiation field for the photochemical model is calculated for diurnally averaged conditions for an assumed (arbitrary) 24 hr rotation period at 30° latitude at vernal equinox, with an assumed zero axial tilt for the planet. These assumptions should provide acceptable "global average" conditions for most young Jupiters.

As is standard in 1D photochemical models, we assume that vertical transport occurs through molecular and "eddy" diffusion, with the eddy diffusion coefficient profile $K_{zz}(z)$ being a free parameter. The molecular diffusion coefficients assumed in the model are described in Moses et al. (2000). Although vertical transport of constituents in real atmospheres
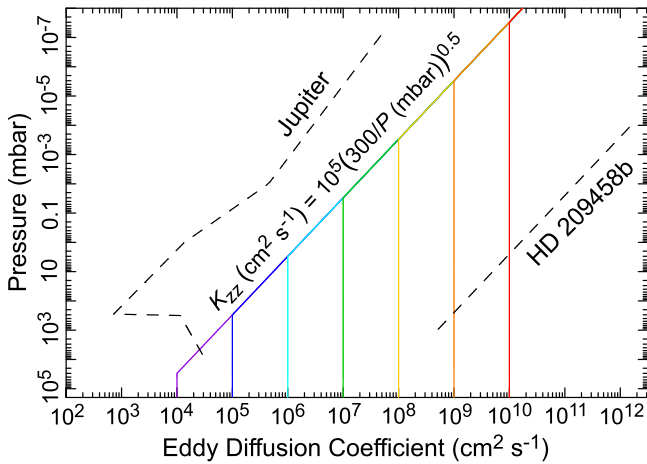
Figure 2. Eddy diffusion coefficient profiles (colored solid lines) adopted in our thermo/photochemical kinetics and transport models. The K_{zz} profiles are assumed to vary as $10^5(300/P_{mbar})^{0.5}$ cm^2 s^{-1} in the radiative region, with different models having different cutoff values (K_{deep}) at depth. Profiles derived for Jupiter (Moses et al. 2005) and the hot Jupiter HD 209458b (Parmentier et al. 2013) are shown for comparison (dashed lines).

occurs through convection, large-scale advection, atmospheric waves, and turbulent "eddies" of all scales, this constituent transport often mimics diffusion (Lindzen 1981; Strobel 1981; Brasseur et al. 1999), and the concept of eddy diffusion has proven to be a useful one for atmospheric models. The eddy diffusion coefficient profile for an atmosphere cannot typically be derived accurately from first principles. Instead, observations of chemically long-lived species are used to empirically constrain $K_{zz}(z)$ (e.g., Allen et al. 1981; Atreya et al. 1984; Moses et al. 2005). On H$_2$-dominated planets and brown dwarfs, the relative abundance of CO and CH$_4$ can be used to constrain K_{zz} at the quench point (see Prinn & Barshay 1977; Fegley & Lodders 1994; Griffith & Yelle 1999; Visscher & Moses 2011). For most directly imaged planets planets, the CO–CH$_4$ quench point will reside in the deep, convective portion of the atmosphere, where free-convection and mixing-length theories (e.g., Stone 1976) predict relatively large eddy diffusion coefficients and rapid mixing (e.g., $K_{zz} \gtrsim 10^{10}$ cm^2 s^{-1} for most young Jupiters, assuming the atmospheric scale height as the mixing length). However, the mixing length to use for these expressions is not obvious (Smith 1998; Freytag et al. 2010), and the quench point for some planets may approach the radiative region, where K_{zz} is expected to drop off significantly before increasing roughly with the inverse square root of atmospheric pressure due to the action of atmospheric waves (e.g., Lindzen 1981; Strobel 1981; Parmentier et al. 2013).

We therefore explore a range of possible K_{zz} profiles, with roughly constant values at depth, trending to values that vary as $1/\sqrt{P}$ as the pressure P decreases. In particular, we assume that K_{zz} (cm^2 s^{-1}) $= 10^5(300/P_{mbar})^{0.5}$ in the radiative region above $\sim$300 mbar (hereafter called the stratosphere), but we do not let K_{zz} drop below some value "K_{deep}" that varies with the different models considered (see Figure 2). This convention allows the different models for a given T_{eff} to have a similar homopause pressure level in the upper atmosphere (i.e., the pressure level to which the molecular species can be mixed before molecular diffusion starts to limit their abundance), while still testing the effect of variations in K_{zz} at the quench point.

Note from Figure 2 that we have chosen stratospheric K_{zz} profiles that are intermediate between those derived empirically from chemical tracers for our own solar-system (cold) Jupiter (Moses et al. 2005) and those derived from tracer transport in 3D dynamical models of the hot transiting exoplanet HD 209458b (Parmentier et al. 2013), which seems reasonable given that atmospheric temperatures for directly imaged planets are intermediate between the two. Eddy diffusion coefficients scale directly with vertical velocities and atmospheric length scales, and both tend to be larger for higher temperatures. Young Jupiters are very hot and convective at depth, but their stratospheres are relatively cold and statically stable.

When estimating K_{zz} profiles for exoplanetary atmospheres, we keep in mind that atmospheric waves are typically responsible for mixing in the stratosphere (e.g., Lindzen 1981), and wave activity could be correlated with both the strength of stellar insolation and internal heat, as the main drivers for these waves. In the troposphere, convection dominates, and mixing is stronger for higher internal heat fluxes. For example, in the Freytag et al. (2010) hydrodynamic models of cool dwarfs, the maximum effective tropospheric diffusion coefficient (analogous to our "K_{deep}") increases with increasing T_{eff} over the whole $900 \leqslant T_{eff} \leqslant 2800$ K model range examined. Freytag et al. (2010) also find that the effective diffusion coefficients in the stratosphere, where convectively excited gravity waves are responsible for atmospheric mixing, also increase with increasing T_{eff} for $T_{eff} \leqslant 1500$ K and $T_{eff} \geqslant 2000$ K, but the behavior at intermediate $1500 < T_{eff} < 2000$ K becomes more complicated due to the effects of clouds, which alter atmospheric stability. At the base of the stratosphere in the Freytag et al. (2010) models, the effective diffusion coefficient goes through a minimum. The K_{zz} profiles are also sensitive to gravity and the overall static stability in the atmosphere. Without running realistic dynamical models for the planets in question, we cannot reliably estimate K_{zz} profiles a priori, and we caution that our empirical profiles may have different magnitudes or functional forms than those of the real young-Jupiter atmospheres. In particular, our profiles do not have the very weak K_{zz} minimum that might be expected at the base of the stratosphere on young Jupiters. Because this minimum K_{zz} results in maximum column abundances for photochemical species produced at high altitudes (e.g., Bézard et al. 2002), our convention may cause us to underestimate the abundances of photochemical products, but not as severely as if we assumed that K_{zz} were constant throughout the atmosphere.

The photochemical model results also depend on the host star's ultraviolet flux and spectral energy distribution (e.g., Venot et al. 2013; Miguel & Kaltenegger 2014; Miguel et al. 2015). For our specific exoplanet models, both 51 Eri (spectral type F0) and HR 8799 (spectral type A5) are expected to be brighter than the Sun at UV wavelengths (see Figure 3). However, the only direct ultraviolet spectral observations we could find for either star are derived from *International Ultraviolet Explorer* (*IUE*) satellite observations of 51 Eri in the MAST archive (http://archive.stsci.edu). Therefore, except for these *IUE* observations, our assumed stellar spectra are assembled from a variety of theoretical sources. For wavelengths greater than 1979 Å, the 51 Eri spectrum is taken from the Heap & Lindler (2011) NextGen model for 51 Eri (HD 29391); for wavelengths between 1200 and 1978.72 Å–except right at H Lyα—we use *IUE* observations of 51 Eri from the MAST *IUE* archive; for wavelengths less than $\sim$1150 Å, we
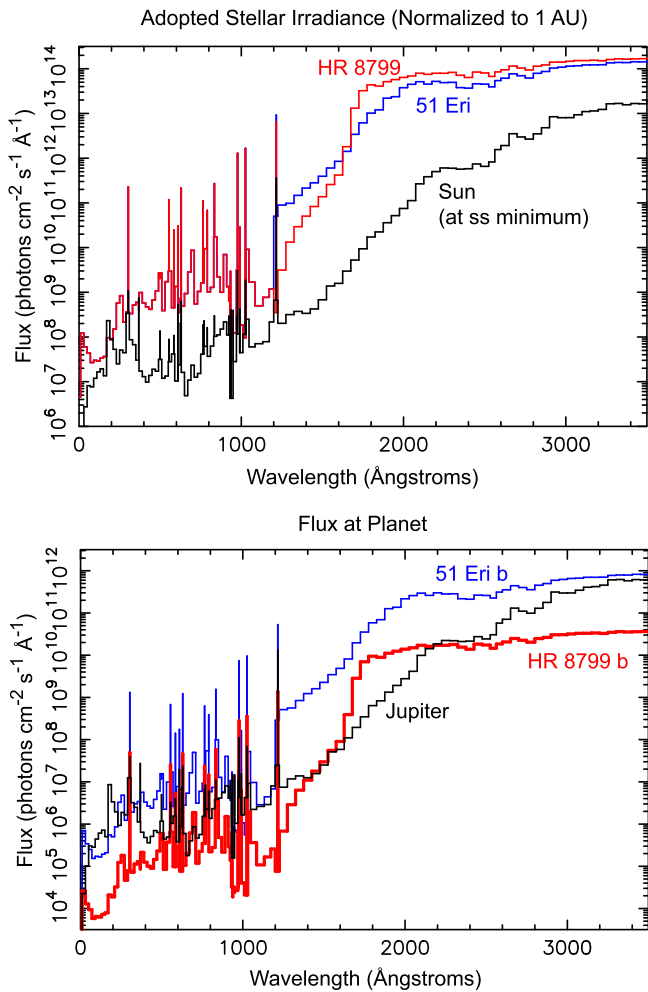
Figure 3. Ultraviolet stellar irradiance adopted in the models. (Top) The irradiance of 51 Eri (blue) and HR 8799 (red) as received at 1 au, in comparison with that the Sun (black); (Bottom) the irradiance at the top of the planet's atmosphere for 51 Eri b (blue) and HR 8799 b (red) in comparison with Jupiter (black). Note from the top panel that both 51 Eri and HR 8799 are brighter than the Sun in the ultraviolet, but 51 Eri b and HR 8799 b are farther away from their host stars than Jupiter, so in terms of the H Lyα flux received, which drives much of the interesting photochemistry, Jupiter receives a flux intermediate between 51 Eri b and HR 8799 b (bottom panel).

adopt the theoretical spectrum of HR 8799 (as the closest analog star) from the Sanz-Forcada et al. (2011) X-exoplanets archive; and for Lyα at 1215.7 Å, we adopt the reconstructed intrinsic H Lyα flux for 51 Eri from Landsman & Simon (1993). The HR 8799 spectrum is a composite of several theoretical models. At wavelengths less than 1150 Å and in the wavelength bin at 1190 Å, the HR 8799 spectrum is from the aforementioned Sanz-Forcada et al. (2011) model of HR 8799; at wavelengths greater than 1150 Å—except for the wavelength bins at 1190 and 1215.7 Å—we use a Castelli & Kurucz (2004) model with assumed parameters of $T_{eff} = 7500$ K, $\log(g) = 4.5$ (cgs), $\log[Fe/H] = -0.5$, radius $= 1.44 R_\odot$; and for 1215.7 Å, we estimate the flux as the average of four stars (κ^2 Tau [A7V], HR 1507 [F0V], 30 LMi [F0V], α Hyi [F0V]) from the Landsman & Simon (1993) database of reconstructed intrinsic H Lyα fluxes, after scaling appropriately for stellar distance. For the spectral irradiance of the Sun shown in Figure 3, we adopt the solar-cycle minimum spectrum of Woods & Rottman (2002).

Note from Figure 3 that 51 Eri and HR 8799 are intrinsically brighter than the Sun in the ultraviolet. Despite the great orbital distances of the HR 8799 planets (b at ~68 au, c at ~43 au, d at ~27 au; cf. Marois et al. 2008 & Maire et al. 2015) and 51 Eri b (14 au according to De Rosa et al. 2015, although we used 13.2 au for the calculations based on the earlier report by Macintosh et al. 2015), these planets—like the giant planets within our own solar system—receive sufficient ultraviolet flux that photochemistry should be effective. In fact, 51 Eri b receives a greater H Lyα flux than any of our solar-system giant planets, including Jupiter (see Figure 3), while the most distant HR 8799 b receives a greater H Ly α flux than either Uranus or Neptune, which both have rich stratospheric hydrocarbon photochemistry (Summers & Strobel 1989; Romani et al. 1993; Moses et al. 1995; Dobrijevic et al. 2010; Orton et al. 2014). Indeed, the first investigation into the photochemistry of 51 Eri b (Zahnle et al. 2016) suggests that photochemical production of complex hydrocarbons and sulfur species will be important on this young Jupiter and may lead to the formation of sulfur and hydrocarbon hazes.

3. RESULTS

Results from our thermo/photochemical kinetics and transport model are presented below. We first discuss the results for generic directly imaged planets, including trends as a function of T_{eff}, $\log(g)$, K_{deep}, and distance from the host star (see also Zahnle & Marley 2014). The relevant disequilibrium chemistry that could potentially affect the spectral appearance of young Jupiters is described. Then, we present specific models for HR 8799 b and 51 Eri b and compare to observations. Note that the model abundance profiles for both the generic and specific planets discussed below are available as supporting material.

3.1. Generic Directly Imaged Planets: Chemistry

For our "generic" young Jupiters, we generate a suite of models for nine different effective temperatures (T_{eff} ranging from 600 K to 1400 K, at 100 K intervals), seven different eddy diffusion coefficient profiles (see Figure 2), and two different surface gravities ($g = 10^{3.5}$ and 10^4 cm s^{-2}). The thermal profiles of these models are shown in Figure 1. Note from Figure 1 that all the models have deep atmospheres that lie within the CO stability field, whereas all but the hottest models switch over to the CH$_4$ stability field in the upper atmosphere. Therefore, if the atmosphere were to remain in chemical equilibrium, CH$_4$ would be the dominant carbon constituent at "photospheric" pressures in the 10^3–0.1 mbar range for most of these planets, and methane absorption would be prominent in the near-infrared emission spectra. However, CO $\leftrightarrows$ CH$_4$ chemical equilibrium cannot be maintained at temperatures $\lesssim$1300 K for any reasonable assumption about the eddy diffusion coefficient profile (e.g., Visscher & Moses 2011), and quenching will occur in the deep, convective regions of these planets. For all the thermal profiles investigated, the CO–CH$_4$ quench point occurs within the CO stability field, and the quenched abundance of CO will be greater than that of CH$_4$.
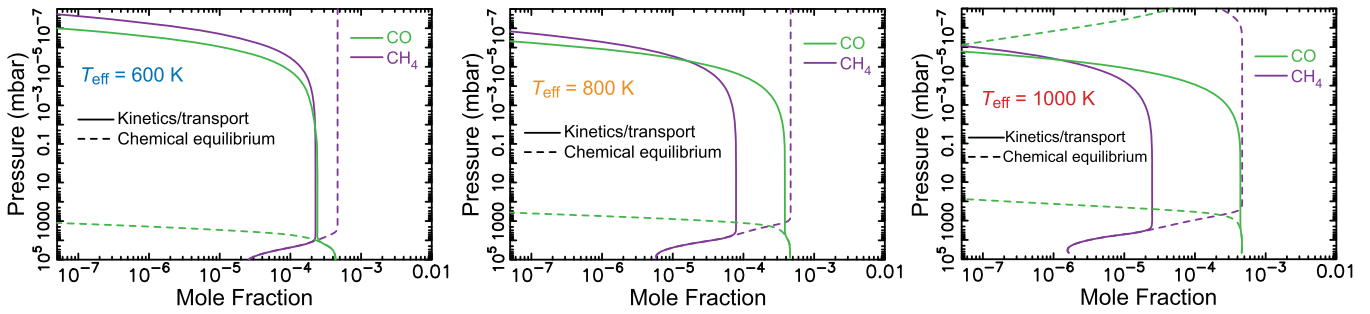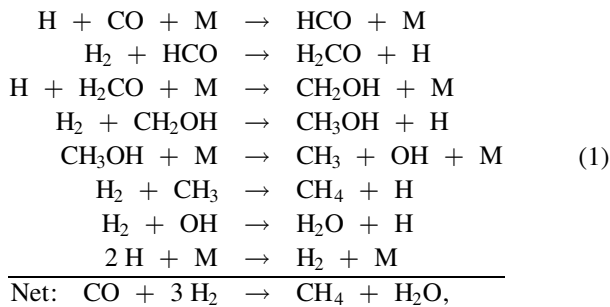
Figure 4. The vertical mixing-ratio profiles of CH_4 (purple) and CO (green) for planets with a surface gravity $\log(g) = 4$ (cgs), a moderate eddy mixing $K_{deep} = 10^7$ cm^2 s^{-1}, and $T_{eff} = 600$ K (Left), 800 K (Middle), 1000 K (Right). Results for chemical equilibrium are shown with dashed lines, and results from our thermo/photochemical kinetics and transport model are shown as solid lines. Note that CH_4 dominates in the observable portion of the atmosphere in chemical equilibrium, whereas CO dominates in the disequilibrium models. The CH_4/CO ratio is strongly dependent on temperature for both types of chemistry, with a higher CH_4/CO ratio being favored for cooler planets.

The dominant kinetic reaction scheme converting CO to CH_4 near the quench point in our models is

$$
\begin{aligned}
H + CO + M &\rightarrow HCO + M \\
H_2 + HCO &\rightarrow H_2CO + H \\
H + H_2CO + M &\rightarrow CH_2OH + M \\
H_2 + CH_2OH &\rightarrow CH_3OH + H \\
CH_3OH + M &\rightarrow CH_3 + OH + M \quad (1) \\
H_2 + CH_3 &\rightarrow CH_4 + H \\
H_2 + OH &\rightarrow H_2O + H \\
2H + M &\rightarrow H_2 + M \\
\hline
\text{Net:} \quad CO + 3H_2 &\rightarrow CH_4 + H_2O,
\end{aligned}
$$

with M representing any third atmospheric molecule or atom. This scheme is identical to the dominant scheme (15) that Visscher & Moses (2011) propose is controlling the conversion of CO into CH_4 on brown dwarfs and is just the reverse of the scheme (3) that Moses et al. (2011) propose is controlling CH_4 $\rightarrow$ CO quenching on hot Jupiters. The rate-limiting step in the above scheme is the reaction $CH_3OH + M \rightarrow CH_3 + OH + M$, where the rate coefficient is derived from the reverse reaction from Jasper et al. (2007). Our chemical model differs from some others in the literature (e.g., Venot et al. 2012; Zahnle & Marley 2014) in that we adopt a slower rate coefficient for $H + CH_3OH \rightarrow H_2O + CH_3$ based on the ab initio transition-state theory calculations of Moses et al. (2011) & Lendvay et al. (1997), and the discussion of relevant experimental data in Norton & Dryer (1990). However, the rate coefficient for this reaction adopted by Zahnle & Marley (2014) and Zahnle et al. (2016) is slow enough that $CH_3OH + M \rightarrow CH_3 + OH + M$ is usually faster, and hence their quench results are not greatly different from those described here. In any case, quenching is very effective in all the generic young-Jupiter models we investigated, and CO replaces CH_4 as the dominant carbon species in the photospheres of these planets.

3.1.1. CO–CH_4 Quenching as a Function of T_{eff} and K_{zz}

Figure 4 shows how the methane and carbon monoxide abundance vary with the planet's effective temperature (for $T_{eff} = 600$, 800, 1000 K), for both the assumption of chemical equilibrium and from our thermo/photochemical kinetics and transport modeling, for $K_{deep} = 10^7$ cm^2 s^{-1} and $\log(g) = 4$ (cgs). Figure 4 emphasizes just how significantly

thermochemical equilibrium fails in its predictions for the composition of directly imaged planets, underpredicting the CO abundance by many orders of magnitude, and overpredicting the CH_4 abundance. The CO–CH_4 quench point is discernible in the plot—it is the pressure at which the CH_4 and CO mixing ratios stop following the equilibrium profiles and become constant with altitude. For the $T_{eff} = 600$ K planet, the quench point is near the CO = CH_4 equal-abundance curve shown in Figure 1, and carbon monoxide and methane quench at nearly equal abundances. Warmer planets have quench points more solidly within the CO stability field, and so the CO abundance then exceeds that of methane at high altitudes. The quenched CH_4 abundance depends strongly on T_{eff}, decreasing with increasing T_{eff}, when other factors like K_{zz} and g are kept identical. The depletion in both the CO and CH_4 mixing ratios at high altitudes in the disequilibrium models in Figure 4 is due to molecular diffusion, which is dependent on temperature. Planets with a higher T_{eff} have warmer upper atmospheres, causing molecular diffusion to take over at deeper levels. Therefore, warmer planets have homopause levels at higher pressures (lower altitudes), all other things being equal.

The quenched species abundances also depend strongly on K_{deep} and on surface gravity. Figure 5 illustrates this relationship for CO (top row) and CH_4 (bottom row) for a suite of generic young Jupiter models, with the lower-gravity (log $(g) = 3.5$) case being plotted in the left column and the higher-gravity case ($\log(g) = 4.0$) in the right column. Note from Figure 5 that the quenched CH_4 abundance is highly sensitive to both T_{eff} and K_{deep}, and is greatest for low temperatures and weak deep vertical mixing. Higher-gravity planets with the same T_{eff} are cooler at any particular pressure level, so higher g favors increased CH_4 abundance, all other factors being equal. In contrast, high g, low T_{eff}, and low K_{deep} favor *smaller* quenched CO abundances. Note, however, the nearly constant quenched CO mixing ratio over a large swath of parameter space in Figure 5 for these two relatively low surface gravities. The quenched CO mixing ratio is less sensitive than CH_4 to variations in T_{eff}, K_{deep}, and g in this range because CO is dominant at the quench point, and the equilibrium CO mixing ratio is more constant with height through the quench region, whereas the equilibrium CH_4 mixing-ratio profile in this region has a significant vertical gradient.

This is an important point. Disequilibrium chemistry from transport-induced quenching will cause CO—not CH_4—to dominate in the photospheres of virtually all directly imaged young planetary-mass (and planetary-gravity) companions,
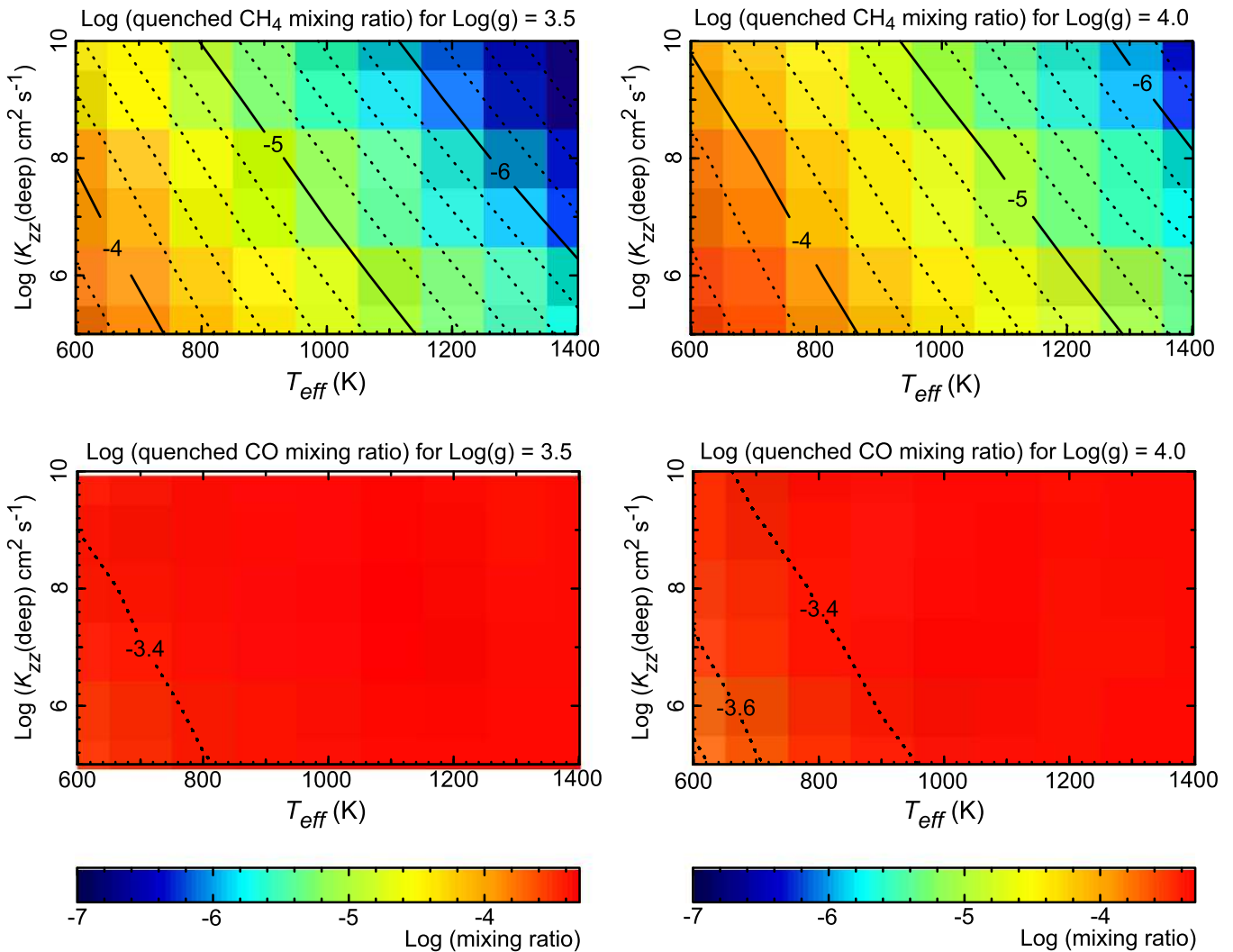
Figure 5. Quenched mixing ratios of CH_4 (top) and CO (bottom) for models with surface gravities of $g = 10^{3.5}$ (left) and 10^4 cm s^{-2} (right) as a function of T_{eff} and K_{deep}. High CH_4 abundances and low CO abundances are favored by small T_{eff}, small K_{deep}, and large g, although the CO abundance is relatively insensitive to these factors over the range of models investigated.

despite the equilibrium predictions for the predominance of CH_4; in addition, the CO abundance should be similar for directly imaged planets with the same metallicity. Spectral signatures of CO should therefore be common for young Jupiters, and derived CO abundances can help constrain the planet's metallicity. Note that this conclusion changes for higher-gravity ($g \gtrsim 10^5$ cm s^{-2}) T dwarfs in this temperature range (Hubeny & Burrows 2007; Zahnle & Marley 2014), where CH_4 can dominate and CO is the minor species.

3.1.2. Sensitivity of Disequilibrium Chemistry to K_{zz}

Figure 6 illustrates how the abundances of several constituents change with the different eddy diffusion coefficient profiles shown in Figure 2, for a model with $T_{eff} = 1000$ K, $\log(g) = 4.0$, and an orbital distance of 68 au from a star with the properties of HR 8799. As the eddy diffusion coefficient at depth, K_{deep}, is increased, vertical transport begins to dominate at greater and greater depths over the chemical kinetic reactions that act to maintain equilibrium. Smaller K_{deep} values lead to mixing ratio profiles that follow the equilibrium profiles to higher altitudes before quenching

occurs. The quenched methane abundance therefore increases with decreasing K_{deep}, and species that are produced through the photochemical destruction of methane, like C_2H_2 and C_2H_6, also have mixing ratios that increase with decreasing K_{deep}. Conversely, the quenched CO abundance decreases with decreasing K_{deep}, but because the chemical equilibrium abundance of CO is only slightly decreasing with altitude over the range of quench points for the different K_{deep} values investigated, the quenched CO mixing ratio is relatively insensitive to K_{deep}.

Water quenches via reaction scheme (1) above at the same point as that of CO and CH_4. Since the equilibrium mixing ratio for H_2O is increasing with increasing altitude very slightly over the pressure range of the quench points, the quenched H_2O abundance very slightly increases with decreasing K_{deep}. Water is a key opacity source in young Jupiters that affects how efficiently heat is lost from the planet, so it is important to keep in mind that the resulting quenched water mixing ratio on directly imaged planets can be a factor of a few below that of chemical-equilibrium predictions in the photosphere. This quenching of H_2O becomes more important for higher T_{eff}, larger K_{deep}, and lower surface gravities. Quenching of water
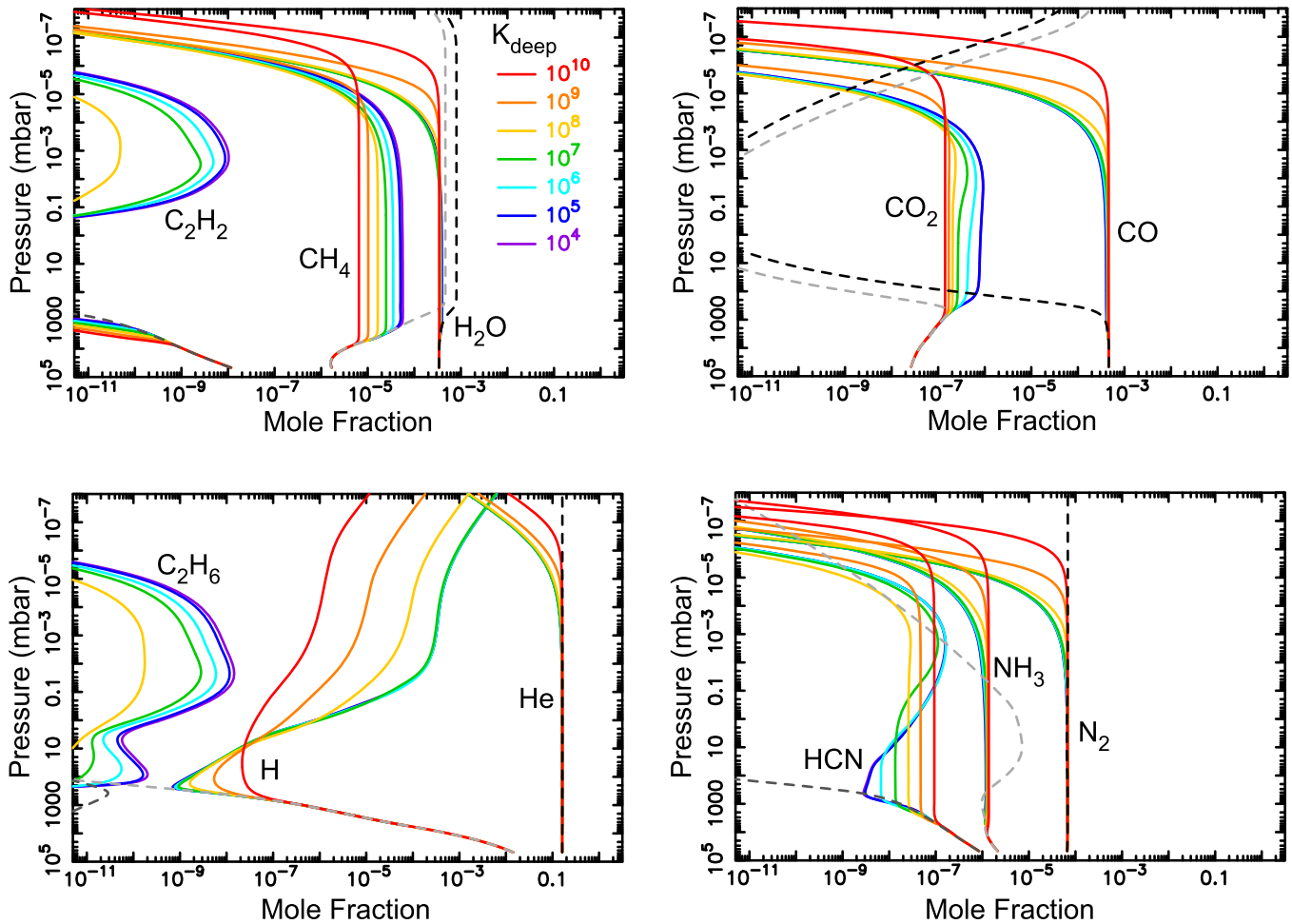
Figure 6. Vertical profiles of several important species in our thermo/photochemical kinetics and transport models (solid colored lines) and in chemical equilibrium (dashed gray and black lines) for a planet with $T_{eff} = 1000$ K and $g = 10^4$ cm s^{-2}, at a distance of 68 au from a star with properties like HR 8799 (Figure 3), as a function of K_{deep} (see the legend in the top left panel, and the K_{zz} profiles shown in Figure 2). Note that the atmosphere is far out of equilibrium for all the eddy diffusion coefficient profiles considered. The quenched CH$_4$ mixing ratio increases with decreasing K_{deep}. The mixing ratios of methane photochemical products such as C$_2$H$_2$, C$_2$H$_6$, and H also increase with decreasing K_{deep}. Water quenches at the same time as CO and CH$_4$, remaining in disequilibrium in the photosphere. Species like HCN and CO$_2$ are affected both by photochemistry and by quenching of the major carbon, oxygen, and nitrogen species.

should therefore be considered in models that calculate the thermal evolution of brown dwarfs and directly imaged planets, particularly for young, small, hot objects.

The NH$_3$-N$_2$ quench point is deeper than that of CO–CH$_4$-H$_2$O. For all the planets considered, this major nitrogen-species quench point is well within the N$_2$-dominated regime, so N$_2$ dominates in the photosphere, and NH$_3$ is less abundant. The equilibrium profiles are not strongly sloped in the quench region, so the quenched abundances of NH$_3$—and N$_2$ in particular—are not very sensitive to K_{deep} (see Figure 6). The dominant quenching scheme for N$_2 \rightarrow$ NH$_3$ in our generic young-Jupiter models is

$$
\begin{aligned}
\mathrm{H} + \mathrm{N_2} + \mathrm{M} &\rightarrow \mathrm{N_2H} + \mathrm{M} \\
\mathrm{H_2} + \mathrm{N_2H} &\rightarrow \mathrm{N_2H_2} + \mathrm{H} \\
\mathrm{H} + \mathrm{N_2H_2} &\rightarrow \mathrm{NH} + \mathrm{NH_2} \\
\mathrm{H_2} + \mathrm{NH} &\rightarrow \mathrm{NH_2} + \mathrm{H} \\
2\,(\mathrm{H_2} + \mathrm{NH_2} &\rightarrow \mathrm{NH_3} + \mathrm{H}) \\
2\,\mathrm{H} + \mathrm{M} &\rightarrow \mathrm{H_2} + \mathrm{M} \\
\hline
\mathrm{Net:}\quad \mathrm{N_2} + 3\,\mathrm{H_2} &\rightarrow 2\,\mathrm{NH_3},
\end{aligned}
\tag{2}
$$

which is simply the reverse of reaction scheme (5) for NH$_3 \rightarrow$ N$_2$ quenching discussed in Moses et al. (2011). The rate-limiting step in the above scheme is the reaction H + N$_2$H$_2 \rightarrow$ NH + NH$_2$, where the rate coefficient derives from the reverse reaction, as determined by Klippenstein et al. (2009).

Constituents such as HCN and CO$_2$ are affected both by photochemistry and by quenching of the dominant carbon, nitrogen, and oxygen carriers (H$_2$O, CO, CH$_4$, NH$_3$, and N$_2$) and thus exhibit complicated vertical profiles in Figure 6. For large values of $K_{zz}(z)$, transport controls the HCN and CO$_2$ profiles throughout the atmospheric column. The quenched abundance of HCN increases with increasing K_{deep} because the equilibrium profile decreases with height within the quench region. Conversely, the quenched abundance of CO$_2$ decreases with increasing K_{deep} because the equilibrium profile increases with height near the quench point; moreover, the photochemically produced CO$_2$ takes longer to diffuse downward when the stratospheric K_{zz} is smaller, so a larger column abundance can build up. In fact, at higher altitudes with the smaller K_{deep} models, photochemical production of HCN and CO$_2$ can dominate over transport from below, and the resulting mixing-ratio "bulges" in the stratosphere represent the signatures of

that photochemical production. In general, the column-integrated CO_2 abundance increases with decreasing K_{deep}, while that of HCN decreases with decreasing K_{deep}. However, this latter result also depends on the planet's thermal structure and incident ultraviolet flux.

Note that the sharp drop off in the species profiles at high altitudes in Figure 6 is due to molecular diffusion. Because the molecular diffusion coefficient profiles for this thermal structure cross the K_{zz} profiles at relatively high altitudes where the K_{zz} profiles have already transitioned to the $P^{0.5}$ sloped region, the homopause levels for most of the models for any particular species are the same for the different K_{zz} models. However, the CH_4 homopause level is at $\sim 3 \times 10^{-7}$ mbar for the sloped K_{zz} case, and Figure 2 shows that the $K_{deep} = 10^{10}$ cm^2 s^{-1} K_{zz} profile does not reached the sloped K_{zz} portion until pressures less than a few $\times 10^{-8}$ mbar. Therefore, the CH_4 molecular diffusion coefficient crosses the $K_{deep} = 10^{10}$ cm^2 s^{-1} K_{zz} profile at a higher altitude (lower pressure) than the other models, leading to a higher-altitude homopause and CH_4 being carried to higher altitudes in that model than the others. Similarly, the H_2O, NH_3, CO, and N_2 molecular diffusion coefficients cross the sloped K_{zz} profile at pressures between where the $K_{deep} = 10^8$ and 10^9 cm^2 s^{-1} models transition to the sloped case, so both the $K_{zz} = 10^9$ and 10^{10} cm^2 s^{-1} cases have higher-altitude H_2O, NH_3, CO, and N_2 homopauses than the other models.

3.1.3. Sensitivity of Disequilibrium Chemistry to Orbital Distance

Figure 7 illustrates how the disequilibrium composition changes as a function of distance from the host star, for planets with $T_{eff} = 1000$ K, $\log(g) = 4.0$ (cgs), $K_{deep} = 10^7$ cm^2 s^{-1}, orbiting at 10, 32, and 100 au from a star with the properties of HR 8799. Because the strong interior heat dominates the energy transport on these young planets, the thermal structures are virtually identical in these cases, so the main differences in the models are due to the incoming ultraviolet flux. The closer a planet is to its star, the greater the UV irradiation received, leading to greater destruction rates of key molecules such as CH_4, NH_3, H_2O, CO, and N_2. That in turn leads to greater production rates of photochemical products such as HCN, CO_2, C_2H_2, C_2H_6, complex hydrocarbons such as methylacetylene (an isomer of C_3H_4) and benzene (an isomer of C_6H_6), complex nitriles such as HC_3N, small oxygen-bearing species such as NO and O_2, and small radicals and atoms such as C, N. O, OH, NH_2, and CH_3.

The dominant photochemical product on young Jupiters is atomic hydrogen. The atomic H is derived largely from water photolysis (producing OH + H), and the subsequent reaction of $OH + H_2 \rightarrow H_2O + H$—a two-step process that catalytically destroys H_2 to produce two H atoms. In this regard, young Jupiters have more in common with close-in transiting giant planets (e.g., Liang et al. 2003) than our solar-system giant planets, and the copious amount of atomic H produced from this photochemistry (see Figure 7) affects much of the subsequent stratospheric chemistry on young Jupiters.

Another key photochemical product is CO_2. Carbon dioxide is produced overwhelmingly from the reaction $OH + CO \rightarrow CO_2 + H$, with the OH deriving from water photolysis. If the stratosphere is relatively warm, as in the example shown in Figure 7 (with a 1 μbar temperature of 377 K), the $OH + H_2 \rightarrow H_2O + H$ reaction occurs at a much faster rate than $OH + CO \rightarrow CO_2 + H$, but the latter reaction provides a slow but steady
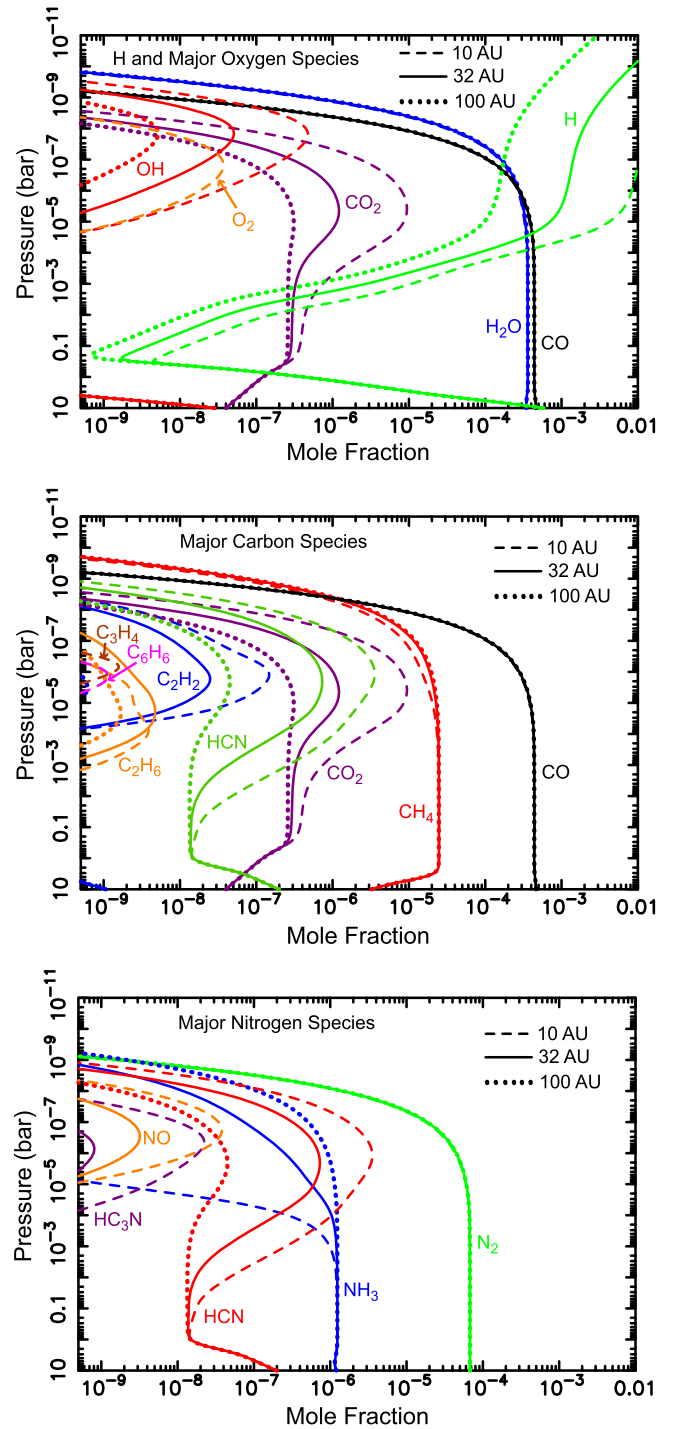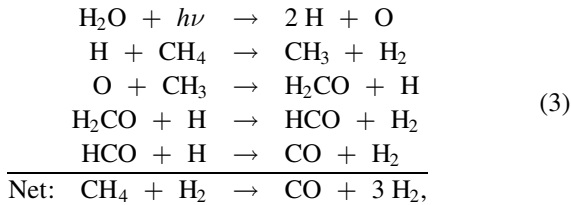

Figure 7. Vertical mixing-ratio profiles of several atmospheric species as a function of orbital distance for a planet with $T_{eff} = 1000$ K, $g = 10^4$ cm s^{-2}, and $K_{deep} = 10^7$ cm^2 s^{-1}, that is being irradiated by an HR 8799-like star at a distance of 10 au (dashed lines), 32 au (solid lines), and 0 au (dotted lines). The greater UV flux received by the closest-in planet leads to increased destruction of photochemically active "parent" molecules such as CH_4, NH_3, H_2O, CO, and N_2, and increased production of photochemical "daughter" products such as HCN, CO_2, complex hydrocarbons, complex nitriles, and atomic species and small radicals.

stream of oxygen away from water and CO into CO_2. Loss of CO_2 occurs through the reverse of the main production reaction (i.e., $H + CO_2 \rightarrow CO + OH$), provided that the upper-atmospheric temperature is warm enough to overcome the

substantial energy barrier for this reaction, as well as through photolysis, through reaction of atomic N to produce NO + CO, and through reaction of CH to produce HCO + CO. Note that all the main loss processes for CO_2 end up recycling the CO. For our generic young Jupiter models, the column-integrated CO_2 production rate exceeds the loss rate, and the photochemically produced CO_2 diffuses down through the atmosphere until it reaches higher-temperature regions where it can once again reach a chemical balance with CO and H_2O. The greater the incident ultraviolet flux, the greater the net photochemical production rate of CO_2 (see Figure 7).

Molecular oxygen becomes a notable high-altitude photochemical product on more highly irradiated young Jupiters. It is produced as a byproduct of the water photochemistry, where photolysis of H_2O produces OH + H and O + 2H, and the OH and O react to form O_2 + H. The O_2 is lost through photolysis (which primarily leads back to H_2O eventually) and through reactions with atomic carbon (which leads to CO).

Some of the CH_4 in the upper atmospheres of young Jupiters will be oxidized to produce CO and eventually CO_2. In our generic young Jupiter models, this process occurs through schemes such as:

$$
\begin{array}{rcl}
H_2O + h\nu & \rightarrow & 2\,H + O \\
H + CH_4 & \rightarrow & CH_3 + H_2 \\
O + CH_3 & \rightarrow & H_2CO + H \\
H_2CO + H & \rightarrow & HCO + H_2 \\
HCO + H & \rightarrow & CO + H_2 \\
\hline
\text{Net:} \quad CH_4 + H_2 & \rightarrow & CO + 3\,H_2,
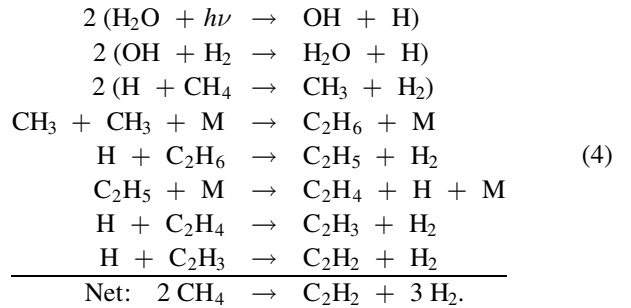\end{array} \tag{3}
$$

with $h\nu$ representing an ultraviolet photon. Methane oxidation schemes such as the one above are more effective the higher the incident stellar ultraviolet flux.

As on the giant planets in our own solar system (e.g., Strobel 1983; Atreya & Romani 1985; Yung & DeMore 1999; Moses et al. 2004; Fouchet et al. 2009), the reduced hydrocarbon photochemistry in the atmospheres of young Jupiters will be efficacious and complex. However, the overall column abundance of the hydrocarbon species produced by neutral photochemistry (as opposed to ion chemistry) on young Jupiters will typically be smaller than on our own giant planets, as a result of the greater stratospheric temperatures, greater stratospheric water abundance, and different dominant and/or competing kinetic reactions, including methane recycling and oxidation. The typically smaller CH_4 mixing ratio on young Jupiters (due to quenching) also contributes to the differences, as does a potentially larger stratospheric eddy K_{zz} coefficient (due to upwardly propagating atmospheric waves generated in the rapidly convecting deep atmospheres of young Jupiters), which allows the high-altitude hydrocarbon photochemical products to be transported more rapidly to the deeper, high-temperature regions, where they become unstable. However, the larger stratospheric temperatures and resulting decreased stability of the complex hydrocarbons play a larger role.

As an example, the column abundance of ethane (C_2H_6) above 100 mbar on Saturn (Moses et al. 2015), which is ~10 au from the Sun, is five orders of magnitude larger than that of the generic 10 au young Jupiter shown in Figure 7, despite the greater H Lyα and overall UV flux received by the 10 au generic young Jupiter around its brighter star. The main source

of the ethane is still the same on both planets—the three-body reaction $CH_3 + CH_3 + M \rightarrow C_2H_6 + M$—but the CH_3 on the 10 au young Jupiter goes back to recycle the CH_4 more than 99.9% of the time, because the higher atmospheric temperatures lead to a more efficient reaction of CH_3 with H_2 to form CH_4 + H. Still, the total stratospheric column production rate of C_2H_6 is larger on the 10 au young Jupiter than on Saturn due to the brightness of the star and the larger UV flux; however, C_2H_6 is also more readily destroyed on the warmer young Jupiter through $H + C_2H_6 \rightarrow C_2H_5 + H_2$, with a much larger percentage of the carbon ending up back in CH_4 rather than in C_2H_x and other higher-order hydrocarbons. On Saturn, the photochemically produced C_2H_6 is much more chemically stable in the colder stratosphere, so the net production rate minus loss rate is greater on Saturn than on the generic 10 au young Jupiter. It is also interesting to note that the direct photolysis of CH_4 on our warmer generic young Jupiters is less important to the production of complex hydrocarbons than the reaction of atomic H with CH_4 to form $CH_3 + H_2$, with the H deriving from H_2O photolysis (see discussion above).

Acetylene (C_2H_2) is also an important photochemical product on our 10 au generic young Jupiter shown in Figure 7 that is produced through reaction schemes such as the following that first go through C_2H_6 and C_2H_4:
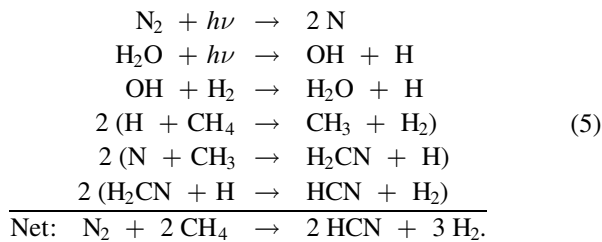
$$
\begin{array}{rcl}
2\,(H_2O + h\nu & \rightarrow & OH + H) \\
2\,(OH + H_2 & \rightarrow & H_2O + H) \\
2\,(H + CH_4 & \rightarrow & CH_3 + H_2) \\
CH_3 + CH_3 + M & \rightarrow & C_2H_6 + M \\
H + C_2H_6 & \rightarrow & C_2H_5 + H_2 \\
C_2H_5 + M & \rightarrow & C_2H_4 + H + M \\
H + C_2H_4 & \rightarrow & C_2H_3 + H_2 \\
H + C_2H_3 & \rightarrow & C_2H_2 + H_2 \\
\hline
\text{Net:} \quad 2\,CH_4 & \rightarrow & C_2H_2 + 3\,H_2.
\end{array} \tag{4}
$$

Acetylene is lost (a) through insertion reactions with atomic C and CH radicals to form C_3H_2 and C_3H_3, (b) through reactions with atomic H to form C_2H_3, with subsequent reactions leading to other C_2H_x species and eventual methane recycling, and (c) by photolysis, which leads predominantly to recycling of the C_2H_2. As on transiting hot Jupiters (Moses et al. 2011), the atomic carbon from loss process (a) here derives both from photolysis of CO and from methane photodestruction to form CH_3, CH_2, and CH, which can react with H to eventually form C.

The relative efficiency of C_3H_2 and C_3H_3 production in some of our more highly irradiated young-Jupiter models (e.g., the 10 au case) is interesting and suggests that complex carbon-rich species like polycyclic aromatic hydrocarbons (PAHs) could potentially form on some directly imaged planets, and might even lead to the condensation of organic hazes in these atmospheres, as enthusiastically advocated by Zahnle et al. (2009, 2016). However, in general, the efficiency of production of refractory organics from simple precursors like C_2H_2, C_2H_6, and C_4H_2 in an H_2-dominated atmosphere seems to have been overestimated by Zahnle et al. (2009), Miller-Ricci Kempton et al. (2012), and Morley et al. (2013)—their arguments would suggest that Jupiter, Saturn, and Neptune should be completely enshrouded in optically thick stratospheric hydrocarbon hazes,

yet that is not the case. Because of a lack of laboratory or theoretical kinetic information on reactions of C_3H_2 and C_3H_3 with other hydrocarbon radicals under relevant low-pressure, reducing conditions, the fate of these C_3H_x species is not obvious (see also Moses et al. 2011; Hébrard et al. 2013). Three-body addition reactions of C_3H_2 and C_3H_3 with abundant ambient H atoms can lead to C_3H_3 and C_3H_4, respectively, and the C_3H_3 can react with CH_3 to form C_4H_6 (Fahr & Nayak 2000; Knyazev & Slagle 2001) or self-react to form various C_6H_6 isomers (Atkinson & Hudgens 1999; Fahr & Nayak 2000), but these three-body reactions are not particularly effective at low pressures. Therefore, C_3H_2 and C_3H_3 build up to mixing ratios of a few $\times\ 10^{-8}$ at high altitudes in our 10 au young-Jupiter model. The comparatively large abundance of C_3H_2 and C_3H_3 radicals here is likely an artifact of having insufficient knowledge of other possible loss mechanisms for these species, and we make a plea for future laboratory experiments or theoretical modeling to rectify this situation.
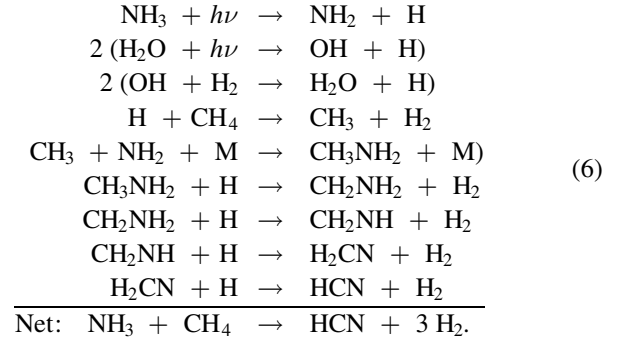
Benzene (C_6H_6) itself is produced in our models through C_3H_3–C_3H_3 recombination, which first goes through a linear C_6H_6 isomer before eventual production of benzene (Fahr & Nayak 2000). The benzene mixing ratio reaches 1 ppb in our 10 au model (see Figure 7), but neither benzene nor any of the other relatively light hydrocarbons considered by our model become abundant enough to achieve saturation and condense. Similarly, the coupled carbon–nitrogen photochemistry in our model leads to non-trivial amounts of complex nitriles such as HC_3N being produced (see Figure 7), but again, these relatively light nitriles never reach saturation. Our neutral chemistry alone does not lead to hazes on these planets. However, we know from Titan that organic hazes can readily form from ion chemistry in a N_2-dominated atmosphere (Imanaka & Smith 2007; Vuitton et al. 2007; Waite et al. 2007; Hörst et al. 2012), and the presence of >10 ppm N_2 in the upper atmospheres of young Jupiters may augment the production of refractory condensable hydrocarbons through Titan-like ion chemistry. This possibility deserves further investigation, both experimentally and theoretically.

The dominant product of the coupled carbon–nitrogen photochemistry is HCN, which forms through hypothesized schemes such as the following:

$$
\begin{array}{rcl}
N_2\ +\ h\nu & \rightarrow & 2\,N \\
H_2O\ +\ h\nu & \rightarrow & OH\ +\ H \\
OH\ +\ H_2 & \rightarrow & H_2O\ +\ H \\
2\,(H\ +\ CH_4 & \rightarrow & CH_3\ +\ H_2) \\
2\,(N\ +\ CH_3 & \rightarrow & H_2CN\ +\ H) \\
2\,(H_2CN\ +\ H & \rightarrow & HCN\ +\ H_2) \\
\hline
\text{Net:}\quad N_2\ +\ 2\,CH_4 & \rightarrow & 2\,HCN\ +\ 3\,H_2.
\end{array}
\tag{5}
$$

Note that N_2, not NH_3, is the source of the nitrogen in this scheme, which is effective at high altitudes. That is why the HCN abundance can exceed the NH_3 abundance at high altitudes in the 10 au model shown in Figure 7. However, NH_3 can also contribute to HCN formation through schemes such as the following that are more effective at lower stratospheric altitudes:

$$
\begin{array}{rcl}
NH_3\ +\ h\nu & \rightarrow & NH_2\ +\ H \\
2\,(H_2O\ +\ h\nu & \rightarrow & OH\ +\ H) \\
2\,(OH\ +\ H_2 & \rightarrow & H_2O\ +\ H) \\
H\ +\ CH_4 & \rightarrow & CH_3\ +\ H_2 \\
CH_3\ +\ NH_2\ +\ M & \rightarrow & CH_3NH_2\ +\ M) \\
CH_3NH_2\ +\ H & \rightarrow & CH_2NH_2\ +\ H_2 \\
CH_2NH_2\ +\ H & \rightarrow & CH_2NH\ +\ H_2 \\
CH_2NH\ +\ H & \rightarrow & H_2CN\ +\ H_2 \\
H_2CN\ +\ H & \rightarrow & HCN\ +\ H_2 \\
\hline
\text{Net:}\quad NH_3\ +\ CH_4 & \rightarrow & HCN\ +\ 3\,H_2.
\end{array}
\tag{6}
$$

As shown in Figure 7, the coupled nitrogen-carbon photochemistry is more efficient with a greater UV flux from the host star.

Molecular nitrogen is fairly stable on young Jupiters. Photodissociation is only effective at wavelengths shorter than $\sim$1000 Å, so N_2 can be shielded to some extent by the more abundant H_2, CO, and H_2O. In addition, the atomic N produced from N_2 photolysis can go back to recycle the N_2, through reactions such as $N + OH \rightarrow NO + H$, followed by $N + NO \rightarrow N_2 + O$. The production rate of NO through this process exceeds the loss rate, and NO appears as a minor high-altitude photochemical product on young Jupiters (Figure 7), especially for higher UV irradiation levels.

Ammonia, on the other hand, is much less stable than N_2 because of weaker bonds, photolysis out to longer wavelengths ($\lambda \lesssim 2300$ Å), efficient reaction with atomic H, and relatively inefficient recycling. The NH_3 photolysis products can end up in N_2 through reactions such as $N + NH_2 \rightarrow NNH + H$, followed by $NNH \rightarrow N_2 + H$, or by $NH_2 + H \rightarrow NH + H_2$, followed by $NH + H \rightarrow N + H_2$, and $N + NO \rightarrow N_2 + O$. The nitrogen in the ammonia can also end up in HCN, through reaction pathways such as scheme (6) above. As is apparent from Figure 7, the NH_3 in the upper stratosphere of young Jupiters becomes more depleted the higher the incident UV flux.

One other nitrogen-bearing photochemical product worth mentioning is HC_3N, which is produced in the model through reaction of atomic N with C_3H_2 and C_3H_3 (e.g., Millar et al. 1991)—speculative reactions that may not be as efficient if we had more information about additional loss processes for these C_3H_x species—and by $CN + C_2H_2 \rightarrow HC_3N + H$ (with the CN from HCN photolysis), which at least has a more convincing pedigree (e.g., Sims et al. 1993). Again, more HC_3N (and CH_3CN) are produced with higher incident UV fluxes. We have not included in the model reactions from the coupled photochemistry of C_2H_2 and NH_3, which can produce a host of complex organic molecules (e.g., Keane et al. 1996; Moses et al. 2010), due to a lack of published thermodynamic properties for these molecules. However, heavier species such as acetaldazine, acetaldehyde hydrazone, and ethylamine may also form on young Jupiters due to this coupled chemistry, particularly on cooler, more highly UV irradiated planets. Unlike on our own solar-system gas giants, hydrazine (N_2H_4) is not a major product of the ammonia photochemistry in our young-Jupiter models because the NH_2 from ammonia photolysis preferentially reacts with the copious amounts of atomic H to produce NH, and eventually N and N_2, or with

CH_3 to form CH_3NH_2 and eventually HCN. On Jupiter and Saturn, the coupled ammonia-methane photochemistry is less efficient due to the lack of CH_3 present in the tropospheric region where NH_3 is photolyzed (e.g., Kaye & Strobel 1983; Moses et al. 2010). However, the hydrazine abundance is very sensitive to temperature and increases significantly as T_{eff} decreases.

3.1.4. Sensitivity of Disequilibrium Chemistry to Temperatures

Finally, many photochemical products on directly imaged planets tend to be very sensitive to temperature—both the effective temperature of the planet, T_{eff} (which on young Jupiters is controlled by the internal heat flux rather than radiation from the host star), and the temperature in the planet's stratosphere (i.e., the radiative region above the convecting troposphere). Note that because irradiation from the host star has less of an effect than internal heat flow on the upper-atmospheric temperatures of these distant, young, hot, directly imaged planets, our generic young-Jupiter models with larger T_{eff} have larger stratospheric temperatures, too (see Figure 1). As discussed previously, T_{eff} affects the quenched abundances of the photochemically active parent molecules, which can in turn influence the production rate of disequilibrium photochemical "daughter" products. More importantly, the stratospheric temperatures affect the subsequent reaction rates of the photochemically produced molecules and radicals, as well as affect the height to which the photochemically active parent molecules are carried before molecular diffusion takes over and severely limits their abundance. The altitude variation of this homopause level can change the pressure at which photolysis occurs, thereby affecting subsequent pressure-dependent reactions. Figure 8 shows how the vertical profiles of some of the major photochemically active molecules in our models vary with temperature, for planets with T_{eff} = 600, 900, or 1200 K, and $\log(g)$ = 3.5 (cgs), K_{deep} = 10^6 cm^2 s^{-1}, orbiting at 68 au from a star with the properties of HR 8799. Although variations in T_{eff} have a relatively straightforward influence on the quenched species' abundances, the response to upper atmospheric temperatures is more complicated.

Smaller T_{eff} results in larger quenched abundances of CH_4, NH_3, and H_2O (all other factors being equal), and allows these molecules to be carried to higher homopause altitudes, so one might naively assume that these factors lead to greater abundances of photochemical products on cooler planets. However, photolysis in these young-Jupiter models is photon-limited rather than species-limited, and the column-integrated photolysis rate of water—which produces H, as well as OH, and thus drives much of the subsequent photochemistry for carbon, nitrogen, and oxygen species—is only slightly different for all three different T_{eff} models shown in Figure 8. Instead, the critical factor is the efficiency of recycling of the parent species versus competing reactions to form other products. When temperatures are larger, recycling of water is more prevalent through reactions such as OH + H_2 → H_2O + H, which has a high energy barrier and operates more effectively at high temperatures. Therefore, fewer reactive OH and O radicals are available to form oxygen-rich photochemical products such as CO_2, H_2CO, CH_3OH, or O_2 when temperatures are higher (see also Zahnle et al. 2016). Moreover, the H atom abundance increases as the upper-atmospheric temperature increases (due to the more efficient catalytic destruction of H_2 following water photolysis), and the increased H atom abundance decreases the
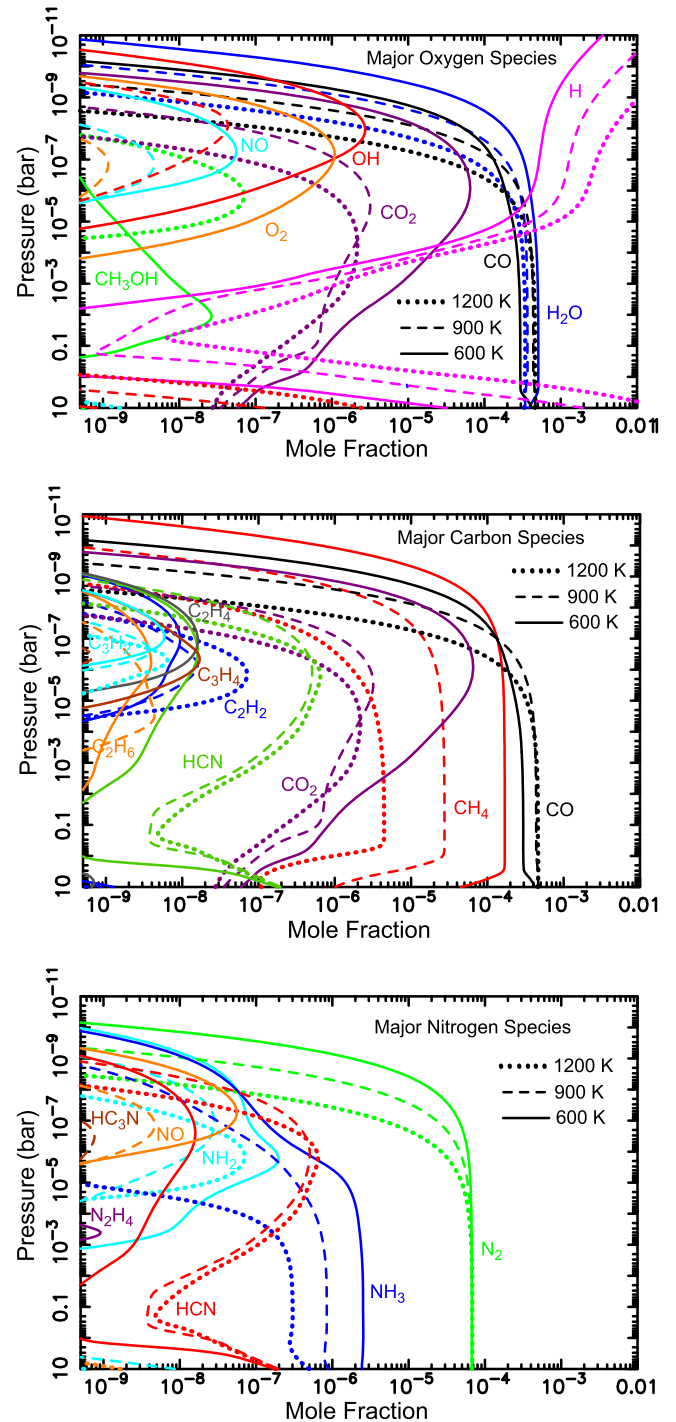

Figure 8. Vertical mixing-ratio profiles of several atmospheric species as a function of T_{eff} for a planet with $g = 10^{3.5}$ cm s^{-2} and $K_{deep} = 10^6$ cm^2 s^{-1}, that is being irradiated by an HR 8799-like star at a distance of 68 au (dashed lines), for T_{eff} = 1200 K (dotted lines), 900 K (dashed lines), and 600 K (solid lines). Most disequilibrium photochemical products are synthesized more effectively in low-T_{eff} atmospheres, but some photochemical products (most notably HCN and C_2H_2) become more abundant at higher T_{eff}.

stability of some photochemical products such as CO_2 and C_2H_6.

On the other hand, the more efficient atomic H production at high temperatures leads to an overall increase in the production rate of reactive CH_3 and NH_2 radicals as the temperature increases, as a result of reactions like H + CH_4 → CH_3 + H_2

and $H + NH_3 \rightarrow NH_2 + H_2$, and even though the reverse recycling reactions are also more effective at high temperatures, the nitrogen- and carbon-bearing products can still form at any temperature. The result is that some photochemical products, like HCN and C_2H_2 that have strong bonds and are more stable at high temperatures, are produced more efficiently at higher T_{eff}, while other species like C_2H_6, C_3H_4, and N_2H_4 are produced more efficiently at lower T_{eff}. The peak production altitude and overall shape of the mixing-ratio profiles can vary with T_{eff}, as well (see Figure 8).

As emphasized by Zahnle et al. (2016), the oxygen-bearing photochemical products are particularly sensitive to the upper-atmospheric temperature, and the abundance of the oxygen species increases significantly when stratospheric temperatures fall below $\sim$250 K. The rate coefficient for the water recycling reaction $OH + H_2 \rightarrow H_2O + H$ drops by almost three orders of magnitude with a reduction in temperature from 500 K to 200 K (Baulch et al. 2005). The reduced efficiency of $OH + H_2 \rightarrow H_2O + H$ at low temperatures opens the door for efficient carbon oxidation, and $CO + OH \rightarrow CO_2 + H$ becomes a competitive loss process for the OH. As a result, neither H_2O nor CO are as efficiently recycled in the colder atmospheres, and the $OH + CO$ reaction will proceed effectively until it depletes enough CO that the $OH + H_2$ reaction can again compete as a loss process for the OH. One then sees a depletion of H_2O and CO at high altitudes in the coldest models, with a concomitant increase in CO_2 and other oxygen products like O_2 and CH_3OH that can form when OH does not effectively recycle back to water. Carbon dioxide becomes a spectroscopically significant photochemical product on colder young Jupiters (see Section 3.2), and the effect is further magnified the greater the incident UV flux.

Figure 9 provides further details showing how the photochemical products CO_2 (top left), HCN (top right), C_2H_6 (bottom left), and C_2H_2 (bottom right) vary with changes in both T_{eff} and K_{deep}, for planets with $\log(g) = 3.5$ cgs located 68 au from a star like HR 8799. For the shape of the vertical K_{zz} profiles we have assumed (see Figure 2), smaller K_{deep} values also correspond to weaker eddy mixing in the lower stratosphere, which increases the residence time for photochemical products synthesized at higher altitudes, allowing them to build up to larger abundances. Therefore, most photochemical products exhibit increased abundances for smaller K_{deep} values. One exception is HCN, which has a more complicated dependence because larger K_{deep} values favor larger quenched abundances of HCN; i.e., quenching, not just photochemistry, contributes to the overall abundance of HCN. For any particular K_{deep} value, the temperature dependence can be complicated, with CO_2 exhibiting a major increase at the lowest temperatures for the reasons discussed above, C_2H_6 being favored at moderately low temperatures, and C_2H_2 and HCN being favored at $T_{eff} \approx 1200$ K.

In general, hydrocarbons such as C_2H_6 and C_2H_2 are not expected to become abundant enough to be observable on young Jupiters, except potentially for closer-in planets (i.e., those receiving a large UV flux) in combination with a more stagnant (lower K_{zz}) lower stratosphere and an increasingly well-mixed and colder ($\lesssim$250 K) upper stratosphere, in which water recycling is less effective and the resulting H production is reduced. Low upper-atmospheric temperatures favor C_2H_6 over C_2H_2, while higher temperatures favor C_2H_2. The quenched HCN abundance reaches potentially observable abundances of a few $\times 10^{17}$ cm^{-2} above 100 mbar for large K_{deep} ($\gtrsim 10^9$ cm^2 s^{-1}), and a high UV flux combined with moderate T_{eff} of 1100–1300 K would provide an increased photochemical component on top of that that quenched HCN. Carbon dioxide is the big winner from a disequilibrium-chemistry standpoint, with observable quantities (see Section 3.2) of greater than 10^{18} cm^{-2} above 100 mbar being produced through both quenching and photochemistry in all the models studied, with a column abundance greater than 10^{19} cm^{-2} above 100 mbar forming in the planets with cooler, more stagnant lower stratospheres.

3.2. Generic Directly Imaged Planets: Spectra

We show selected spectra from our directly imaged planets in Figures 10 & 11. These synthetic spectra were generated from the forward radiative-transfer model described in Line et al. (2013, 2014, 2015). First, Figure 10 shows results from two generic models with different quenched abundances of CH_4 and CO. Both planets are assumed to be 39 pc from Earth, with surface gravities of 10^4 cm s^{-2}, a radius of $1.2R_J$, and a uniform gray absorbing aerosol layer with a base located where the thermal profile crosses the $MgSiO_3$ condensation curve and a total optical depth of unity between 1 bar and 10^{-4} bars. Both planets are assumed to orbit 68 au from a star with properties of HR 8799. The planet shown in the left panel has $T_{eff} = 600$ K and $K_{deep} = 10^5$ cm^2 s^{-1}, for which the quenched CH_4 mixing ratio is 2.4 times that of CO (see Figure 5). The planet in the right panel has $T_{eff} = 1000$ K and $K_{deep} = 10^7$ cm^2 s^{-1}, such that the quenched CO mixing ratio is 18 times that of CH_4. Absorption features of H_2O are readily apparent in the spectra of both planets in bands near $\sim$1.4, $\sim$1.8–1.9, $\sim$2.6–2.8, and the $\sim$5.5–7.5 μm region, and CO absorption features are apparent in both plots in the $\sim$4.5–4.8 μm region. Although CH_4 absorption features are also obvious in both plots, the bands at 2.3, 3.3, and 7.7 μm are deeper for the cooler planet, with its larger quenched methane abundance. The cooler planet also has a larger column of photochemically produced CO_2, which shows up most distinctly in the 4.2–4.3 μm absorption bands on both planets, as well as more subtly in the 2.7–2.8 μm region on the warmer planet and the $\sim$14–16 μm region on the cooler planet. Absorption in the 4.2–4.3 μm CO_2 bands should be particularly apparent on young Jupiters, trending toward greater absorption for lower T_{eff}. HCN is abundant enough on the warmer, more rapidly mixed planet (see Figure 9) to have a minor effect on the spectrum at 3 μm, while other photochemical products such as C_2H_2 are not abundant enough to notably affect the spectra for either of these generic young Jupiters considered.

Figure 11 further illustrates how the spectra of our generic young Jupiters changes as a function of T_{eff}. In this figure, we plot the synthetic spectra from the photochemical models shown in Figure 8—these planets are assumed to orbit 68 au from a star with properties similar to HR 8799, and have $g = 3200$ cm s^{-2}, $K_{deep} = 10^6$ cm^2 s^{-1}, and $T_{eff} = 600$, 900, or 1200 K. For the spectral calculations, we again assume that the systems are located 39 pc from Earth, with planetary radii $= 1.0R_J$ and uniform gray absorbing clouds with optical depths of one between the base of the $MgSiO_3$ condensation region and the top of the atmosphere. The cooler planet contains more quenched H_2O and CH_4 and possesses a colder stratosphere, so the absorption bands due to these species are therefore deeper. The cooler planet also has more quenched
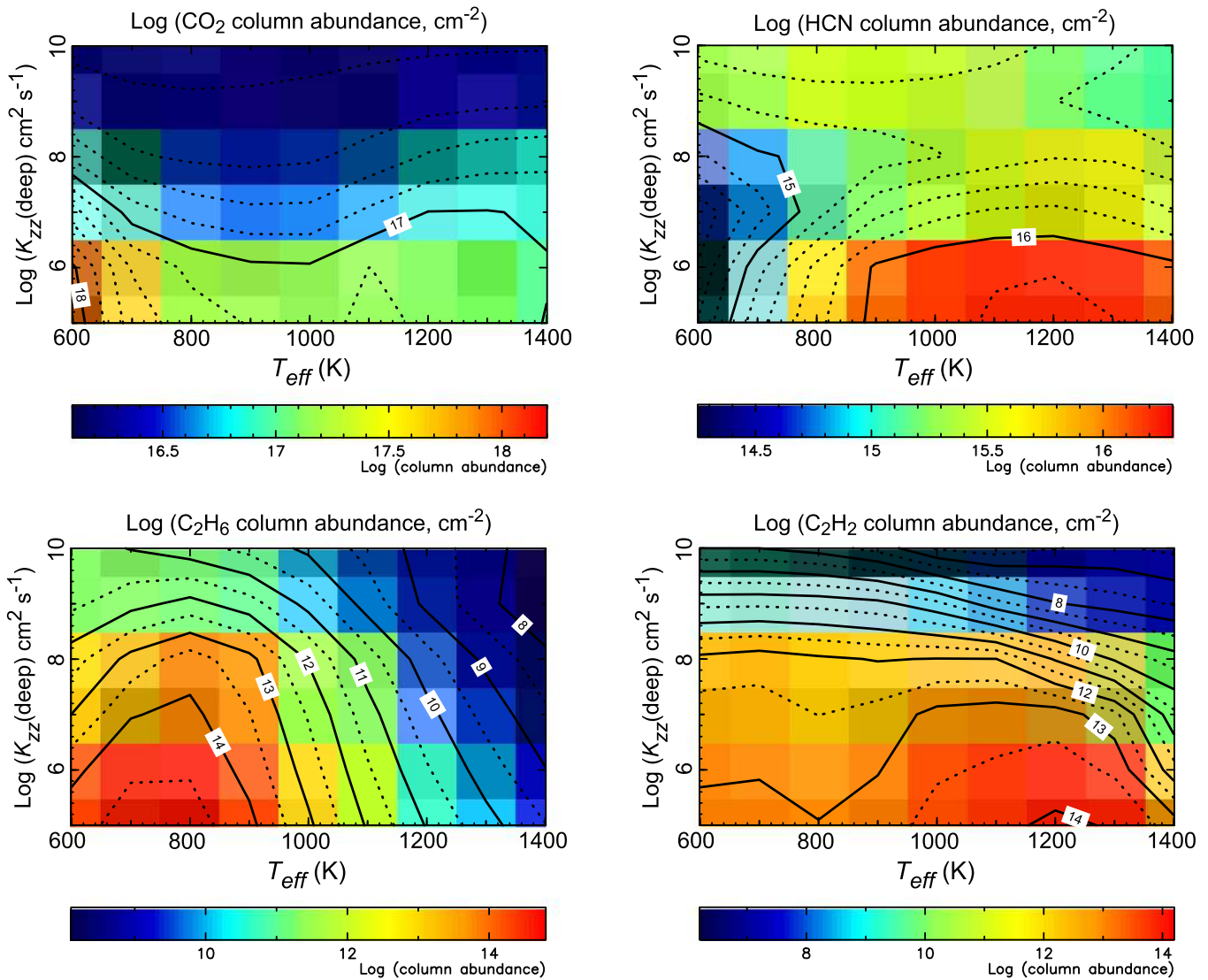
Figure 9. Integrated column abundance of CO_2 (top left), HCN (top right), C_2H_6 (bottom left), and C_2H_2 (bottom right) above 1 mbar as a function of T_{eff} and K_{deep} for planets with a surface gravity of $g = 10^{3.5}$ located at 68 au from a star with the properties of HR 8799. Photochemistry dominates in this region of the atmosphere, and different species exhibit a complicated sensitivity to both T_{eff} and K_{deep}.

NH_3, which shows up readily near 10.4 μm, and more photochemically produced CO_2, which is notable in the 4.2–4.3 and ~15 μm bands.

The influence of photochemically produced CO_2 on the emission spectrum of young Jupiters diminishes strongly with increasing T_{eff} and increasing K_{zz} in the stratosphere, and is, in particular, highly sensitive to the stratospheric temperature, as discussed in Section 3.1.4. For sufficiently large stratospheric K_{zz} and temperatures, an increased UV irradiation level does not overcome the tendency toward small overall CO_2 column abundances. For example, Figure 12 shows how spectra from the $T_{eff} = 1000$ K, $\log(g) = 4.0$, $K_{deep} = 10^7$ cm^2 s^{-1} models from Figure 7 vary with orbital distance ranging from 10, 32, and 100 au. The spectra are similar for all three planets. There is a slight difference in the 4.2–4.3 μm region due to increased CO_2 absorption for the shorter-period planets, but these differences are small. In general, the spectra of young directly imaged giant planets will be dominated by quenched H_2O, CH_4, and CO, but absoption features due to photochemically produced species such as CO_2 can be important when T_{eff} is

small, lower-stratospheric eddy mixing coefficients are small (which allow larger column abundances of photochemical species to build up), and UV irradiation levels are large.

3.3. HR 8799 b

Of the four planets detected in the HR 8799 system (Marois et al. 2008, 2010), HR 8799 b is the farthest away from the host star (68 au, Maire et al. 2015) and seems to be the smallest and coolest (e.g., Marois et al. 2008). Most comparisons of spectral models with observational data favor T_{eff} in the broad range 700–1200 K and $\log(g) = 3.0$–4.5 cgs for HR 8799 b (Marois et al. 2008; Hinz et al. 2010; Barman et al. 2011a, 2015; Currie et al. 2011, 2014; Galicher et al. 2011; Madhusudhan et al. 2011; Marley et al. 2012; Skemer et al. 2012; Ingraham et al. 2014; Rajan et al. 2015). The broad range here stems from degeneracies between T_{eff}, $\log(g)$, assumed cloud properties, planetary radius, and metallicity. Moreover, the models tend to have difficulty simultaneously fitting the short-wavelength infrared spectra (1–2.5 μm), which show evidence for deeper molecular absorptions, and the longer-wavelength mid-infrared
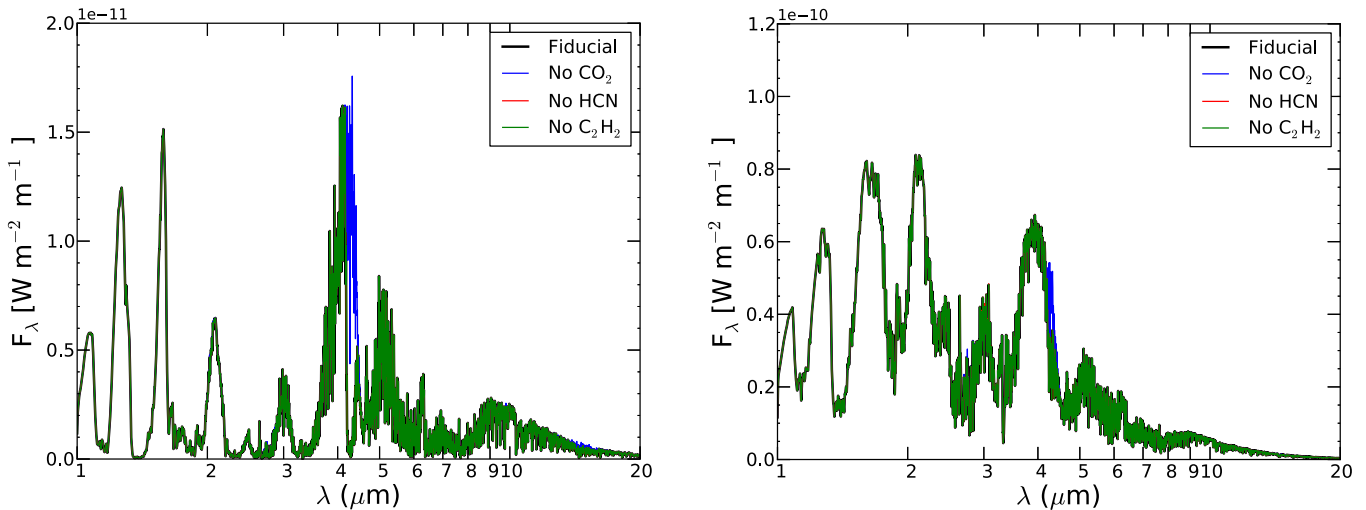
Figure 10. Synthetic spectra from our photochemical models of generic young Jupiters orbiting at 68 au from a star with the properties of HR 8799, with planetary properties of $\log(g) = 4.0$ cgs, $R = 1.2R_J$, a global gray absorbing cloud (no patchiness), at a distance of 39 pc from Earth, for (Left) $T_{eff} = 600$ K and $K_{deep} = 10^5$ cm^2 s^{-1} and (Right) $T_{eff} = 1000$ K and $K_{deep} = 10^7$ cm^2 s^{-1}. The cloud base is assumed to be located at the pressure where the MgSiO$_3$ condensation curve crosses the temperature profile, and the cloud is assumed to extend to the top of the atmosphere, with the opacity adjusted such that the optical depth is unity between 1 and 10^{-4} bars. The plots show how various photochemical products affect the spectra, through the removal of CO$_2$ (blue), HCN (red), and C$_2$H$_2$ (green) from the spectral calculations. Of these photochemical products, only CO$_2$ affects the spectra significantly at near-IR wavelengths.
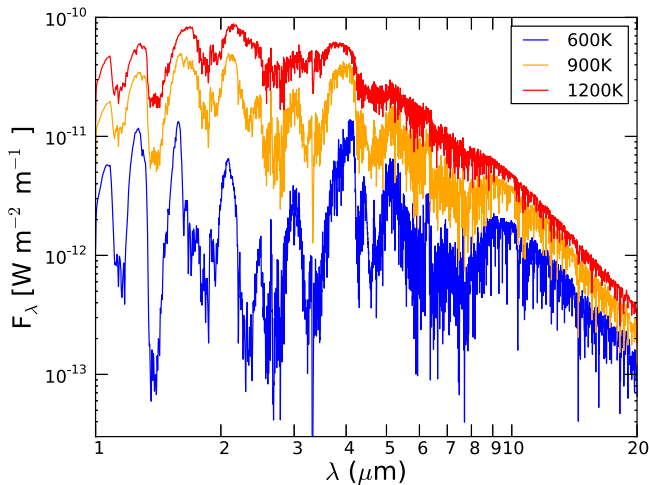

Figure 11. Synthetic spectra from our photochemical models of generic young Jupiters orbiting 68 au from a star with the properties of HR 8799, with surface gravities $g = 3200$ cm s^{-2}, eddy $K_{deep} = 10^6$ cm^2 s^{-1}, and effective temperatures $T_{eff} = 600$ K (blue), 900 K (orange), and 1200 K (red). These models correspond to the ones shown in Figure 8. For the purpose of the spectral calculations, we have assumed that the planets have radii = $1.0R_J$, are located 39 pc from Earth, and possess uniform gray absorbing clouds with optical depths of one between the base of the MgSiO$_3$ condensation region and the top of the atmosphere. Note that the absorption in most of the molecular bands (e.g., H$_2$O, CH$_4$, NH$_3$, and CO$_2$) increases as T_{eff} decreases (cf. Figure 8).

Figure 12. Synthetic spectra from our photochemical models of generic young Jupiters with $T_{eff} = 1000$ K, $g = 10^4$ cm s^{-2}, $K_{deep} = 10^7$ cm^2 s^{-1}, orbiting a star with the properties of HR 8799 at 10 au (red), 32 au (green), and 100 au (blue). These models correspond to the ones shown in Figure 7. For the purpose of the spectral calculations, we have assumed that the planets have radii = $1.2R_J$, are located 39 pc from Earth, and possess uniform gray absorbing clouds with optical depths of one between 1 and 10^{-4} mbar. Note that at this relatively high T_{eff} and K_{deep} the photochemical products have little impact on the spectrum, except for the minor increase in CO$_2$ absorption at 4.2–4.3 μm in the shorter-period model, due to its greater photochemical production and correspondingly larger CO$_2$ abundance.

photometric (3–5 μm), which exhibit flatter spectral behavior. These difficulties complicate the derivation of planetary properties. The best-fit models typically seem to require thick but patchy clouds, and the spectrum of HR 8799 b is distinctly different from brown dwarfs with the same effective temperature.

For our HR 8799 b models, we adopt the recent constraints of Barman et al. (2015) ($T_{eff} = 1000 \pm 100$ K and log $(g) = 3.5 \pm 0.5$ cgs) because their analysis of the medium-resolution H- and K-band data with the OSIRIS instrument at Keck have provided the best available constraints on the
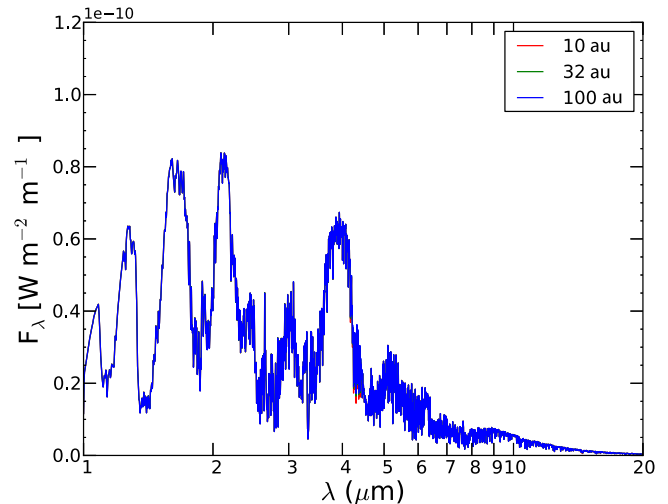
abundances of CH$_4$, H$_2$O, and CO. For consistency with the Barman et al. (2015) modeling procedure and their preferred restriction of C and O abundances to possible sequences derived from the Öberg et al. (2011) disk chemical evolution model, we also adopt a slightly super-solar C/O ratio of 0.65–0.7 for these models, and metallicities of ~0.6–1.0 times solar.

Figure 13 shows the results from one of our HR 8799 b models. In this model, we have assumed $T_{eff} = 1000$ K, $g = 3000$ cm s^{-2} (with assumed mass 1.9M_J), and a solar
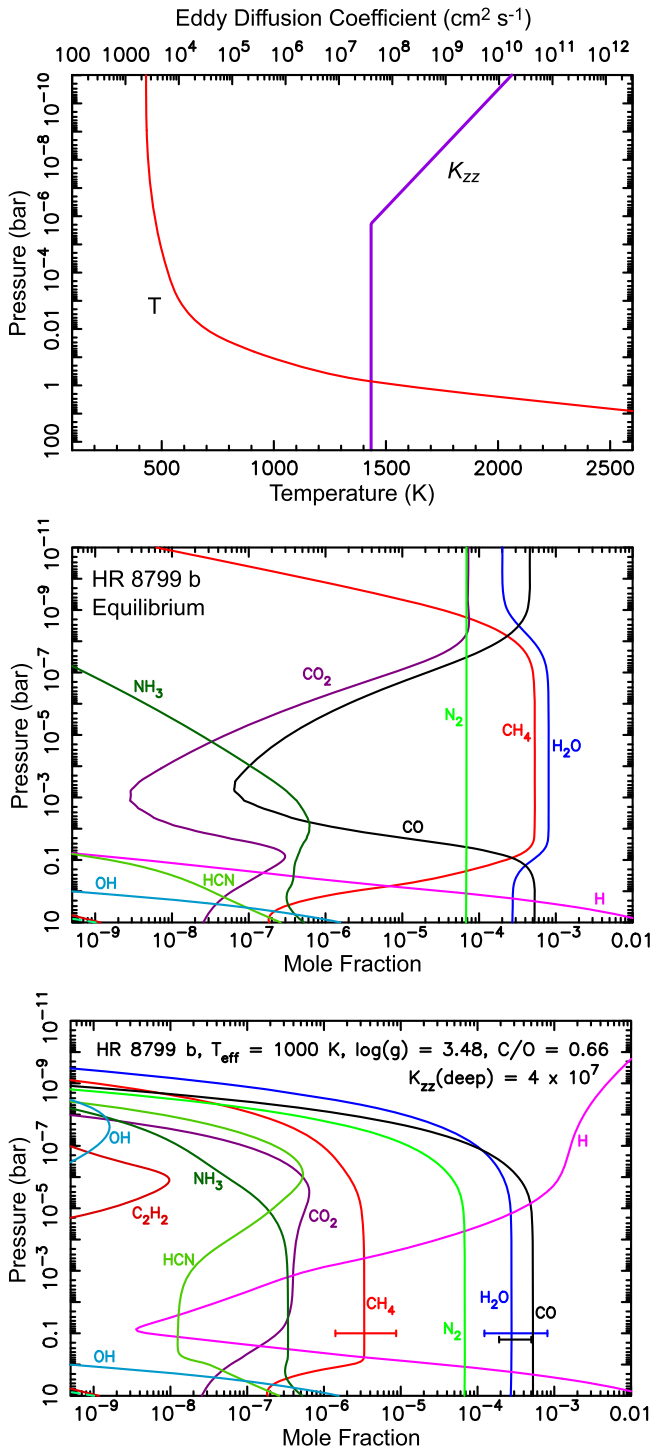
Figure 13. Chemical model for HR 8799 b assuming $T_{eff} = 1000$ K, $g = 3000$ cm s^{-2} (assumed $M = 1.9 M_J$), and solar metallicity, except C/O = 0.66: (Top) The temperature profile (red curve, bottom axis) from the radiative-convective equilibrium model of Marley et al. (2012) assuming the above bulk constraints, and the eddy diffusion coefficient profile (purple curve, top axis) adopted in the photochemical model; (Middle) the predicted thermochemical equilibrium mixing-ratio profiles for the major oxygen, carbon, and nitrogen species, as labeled, for the assumed pressure-temperature profile; (Bottom) mixing-ratio profiles predicted from our thermo/photochemical kinetics and transport model for the above thermal structure, K_{zz} profile, and assumed bulk elemental composition. The line segments in the bottom plot are the observational constraints for CH$_4$ (red), H$_2$O (blue), and CO (black) from Barman et al. (2015).

metallicity atmosphere except for a C/O ratio of 0.66, and we have used the radiative-convective equilibrium model of Marley et al. (2012) to define the temperature structure. With this thermal structure, the quenched CH$_4$ abundance falls within the 1.4×10^{-6}–8.7×10^{-6} mixing-ratio constraints provided by Barman et al. (2015) when $\log(K_{deep}) \approx 6$–9, with a best fit for $K_{deep} = 4 \times 10^7$ cm^2 s^{-1}. Figure 13 demonstrates that the CO mixing ratio is expected to be much larger than the CH$_4$ mixing ratio on HR 8799 b as a result of transport-induced quenching. Similarly, the quenched N$_2$ abundance is much greater than that of NH$_3$, and H$_2$O quenches at a mixing ratio a factor of ~3 smaller than equilibrium predictions. As expected (see Section 3.1), the CO$_2$ and HCN abundances are also significantly enhanced in comparison to chemical equilibrium as a result of quenching of the dominant oxygen, carbon, and nitrogen species (see also Moses et al. 2011). The coupled carbon-oxygen and carbon-nitrogen photochemistry described in Section 3.1) leads to an additional peak in the CO$_2$ and HCN abundances at high altitudes, which for the case of HCN adds notably to the stratospheric column abundance. Hydrocarbons such as C$_2$H$_2$ and C$_2$H$_6$ and key radicals such as OH and NH$_2$ are produced from high-altitude photochemistry, but these species are less stable in the lower stratosphere, and they never reach observable column abundances.

Overall, although disequilibrium quenching is very important in controlling the atmospheric composition of HR 8799 b —including controlling the abundance of minor species not typically considered in simple quenching models—photochemistry itself is less important due to relatively warm stratospheric temperatures (which tend to decrease the stability of photochemical products) and the mild UV flux received by HR 8799 b. If the lower-stratospheric eddy K_{zz} values were much lower than we have assumed here, then the column abundance of key photochemical products like C$_2$H$_x$ hydrocarbons could be increased, although it is still unlikely that they could achieve observable values.

Other HR 8799 b models developed with different assumptions about the thermal structure and other planetary parameters produce similar results. For colder (warmer) thermal structures, it takes a larger (smaller) K_{deep} to quench CH$_4$ at the same abundance as in the above model. As an example, Figure 14 shows the results for two photochemical models that assume $T_{eff} = 1000$ K, $g = 3162$ cm s^{-2}, a C/O ratio of 0.7, a subsolar metallicity (i.e., ~0.63 times the solar O/H of Grevesse et al. 2007), a thermal structure that is taken from Barman et al. (2015), and an assumed K_{deep} that is 10^8 cm^2 s^{-1} (solid curves) or 10^9 cm^2 s^{-1} (dotted curves). These models are cooler everywhere than the one shown in Figure 13, and so it takes a larger K_{deep} to quench CH$_4$ at the same abundance as the previous model. If the eddy diffusion coefficient were to remain high in the stratosphere, as in the models shown here, then the photochemical species produced at high altitudes could diffuse rapidly through the stratosphere to deeper, warmer levels, where they would readily be converted back to the major quenched species. So again, photochemistry does not have much of an effect on the spectroscopically active molecules for these HR 8799 b models. However, transport-induced quenching does play a major role in shaping atmospheric composition, including for the species H$_2$O, CO, CH$_4$, CO$_2$, N$_2$, NH$_3$, and HCN. Quenching on a lower-gravity planet readily explains why the observed CH$_4$ absorption is so
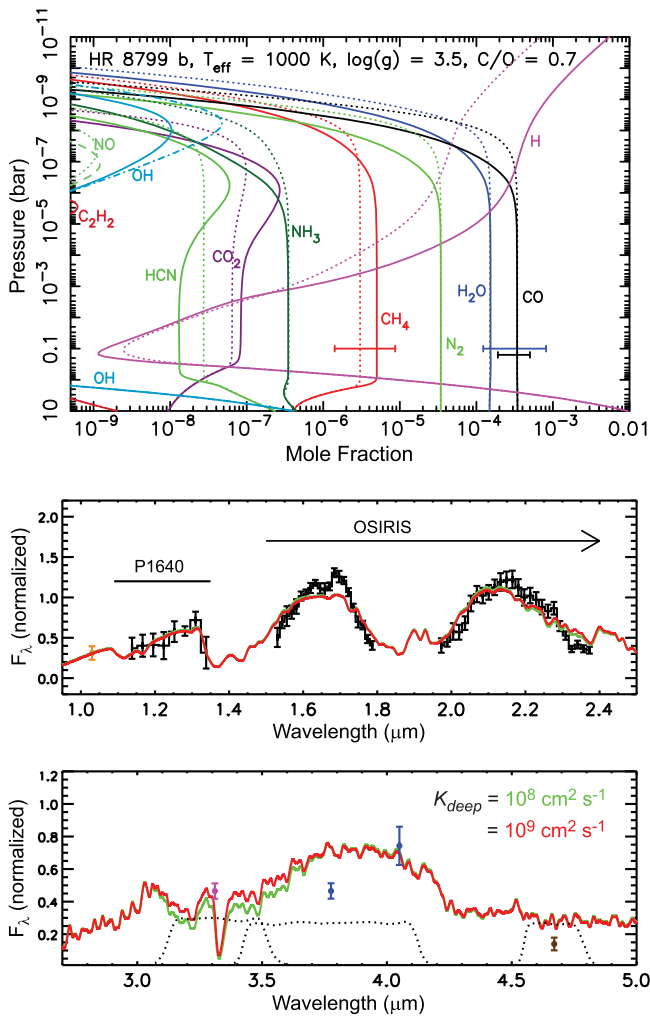
Figure 14. (Top) Model results for HR 8799 b assuming T_{eff} = 1000 K, log (g) = 3.5 cgs, C/O = 0.7, a subsolar metallicity, a temperature profile from Barman et al. (2015), and K_{deep} = 10^8 cm^2 s^{-1}(solid curves) and 10^9 cm^2 s^{-1}(dotted curves). (Bottom two panels) HR 8799 b observations (black data points with error bars; see text) compared with synthetic spectra generated from our thermo/photochemical kinetics and transport models from the top panel, for K_{deep} = 10^8 cm^2 s^{-1} (green) and 10^9 cm^2 s^{-1} (red); see text and Barman et al. (2015) for details.

much less significant on HR 8799 b than on brown dwarfs of similar effective temperatures (see also Barman et al. 2011a, 2015; Zahnle & Marley 2014). Although K_{deep} can in theory be constrained by comparing disequilibrium models like these to observations, in practice the thermal structure of the planet is uncertain enough that firm constraints are not possible. We simply conclude that the deep-atmospheric mixing is strong (K_{deep} > 10^7 cm^2 s^{-1}) on HR 8799 b, consistent with that expected from convection on a planet with a strong internal heat source (e.g., Stone 1976).

Figure 14 also shows how synthetic spectra from these models compare to actual observations. In order of shorter to longer wavelengths in this figure, we plot the z/Y-band flux of Currie et al. (2011) in orange, the low-resolution P1640 J-band spectrum of Oppenheimer et al. (2013) in black, the H -band OSIRIS spectrum of Barman et al. (2011a) in black, the K-band OSIRIS spectrum of Barman et al. (2015) in black, and the longer-wavelength photometric data of Skemer et al. (2012) in pink, Currie et al. (2014) in blue, and Galicher et al. (2011) in

brown. A small scaling was applied to the H -band portion of the P1640 spectrum to get it to match the H -band OSIRIS spectrum, as described in Barman et al. (2015). For other modeling assumptions, see Barman et al. (2015). The quenched CH_4 abundance is sensitive to the assumed deep eddy diffusion coefficient K_{deep}, and Figure 14 shows that in the near-infrared, spectral observations in the 3.1–3.5 μm region are best suited to constraining the methane mixing ratio and hence K_{deep}. Although current ground-based and *Hubble Space Telescope* observations can provide sufficient spectral information to loosely constrain CH_4 and thus K_{deep} (e.g., Konopacky et al. 2013; Barman et al. 2015), model degeneracies will be more easily broken with the broader wavelength coverage and moderate spectral resolution provided by the *James Webb Space Telescope* (*JWST*) or other space-based instrumentation with coronographic spectroscopy capabilities.

The column abundances of key species in our full range of HR 8799 b models are listed in Table 1. Water is the dominant infrared opacity source and is readily detected in HR 8799 b spectra. Methane and carbon monoxide have also been detected (e.g., Barman et al. 2011a, 2015; Currie et al. 2011). Tentative detections of NH_3 and/or C_2H_2, and CO_2 or HCN have been reported by Oppenheimer et al. (2013) in 1.0–1.8 μm spectra of the planet. Many of these tentative detections are inconsistent with our HR 8799 b models. For example, C_2H_2 in our photochemical models never becomes abundant enough to be detectable on HR 8799 b for any of the infrared bands, including the relatively strong ones near 13.6 and ~3 μm. Carbon dioxide in the model is not abundant enough to be detectable in the 1–1.8 μm range, where the bands are weak, but it should be detectable in the stronger bands between 4–4.5 μm and near 15 μm; CO_2 may also be detectable in the ~2.7–2.8 μm range if the photosphere extends down to ~1 bar, but that may be problematic given that clouds are inferred to be present. Hydrogen cyanide is potentially detectable in bands near 2.5, ~3, and 6.8–7.4 μm if the photosphere extends deep, with a more likely stratospheric detection in the 14- μm band; however, HCN is not predicted to be abundant enough to be detectable in the 1–1.8 μm region observed by Oppenheimer et al. (2013). Similarly, if the photosphere extends below ~1 bar, NH_3 may be detectable near ~1.5 μm, ~2 μm, ~3 μm, and ~6.15 μm, but has the best chance of being detected in the stratosphere in the stronger bands in the 9–11 μm region. Methane should be detectable in the ~1.6 and 2.3 μm bands if the obscuring clouds are confined to altitudes below ~100 mbar (and in fact CH_4 has been detected in the 2.3 μm band, Barman et al. 2011a, 2015), with an even better chance of being detected in the stronger 3.3 μm band (see Currie et al. 2011, and Figure 14) and the 7.7 μm band. The CO band in the 4.5–4.9 μm region should produce significant absorption in HR 8799 b spectra, and the band near 2.3–2.4 μm should also be observable (see Barman et al. 2015) and may help constrain cloud heights/thicknesses; however, moderate-resolution spectra are required, as some of the lines in this band overlap with H_2O and CH_4 lines, complicating identification (Barman et al. 2015).

3.4. 51 Eri b

51 Eridani b, a ~20 Myr old exoplanet that is cooler and closer to its star than HR 8799 b, was recently discovered with the Gemini Planet Imager (GPI; Macintosh et al. 2015). As with several other cool young Jupiters, the near-infrared flux

Table 1
Column Abundances for the HR 8799 b Models

Species	Column Abundance Above 10 mbar (cm^{-2})	Column Abundance Above 100 mbar (cm^{-2})	Column Abundance Above 1 bar (cm^{-2})
CH_4	$(2–3) \times 10^{18}$	$(2–3) \times 10^{19}$	$(2–3) \times 10^{20}$
C_2H_2	$(0.01–5) \times 10^{12}$	$(0.01–5) \times 10^{12}$	$(0.8–8) \times 10^{14}$
H_2O	$(1–3) \times 10^{20}$	$(1–3) \times 10^{21}$	$(1–3) \times 10^{22}$
CO	$(2.8–4.6) \times 10^{20}$	$(2.8–4.5) \times 10^{21}$	$(2.8–4.5) \times 10^{22}$
CO_2	$(0.5–4) \times 10^{17}$	$(0.5–3) \times 10^{18}$	$(0.4–1) \times 10^{19}$
NH_3	$(2.5–3) \times 10^{17}$	$(2.5–3) \times 10^{18}$	$(2.5–3) \times 10^{19}$
HCN	$(1–3) \times 10^{16}$	$(1–2.5) \times 10^{17}$	$(1–2.5) \times 10^{18}$

Note. Models assume $\log(g) = 3.47–3.5$ cgs.

and emission spectrum of 51 Eri b is difficult to reproduce theoretically without invoking cloudy or partial-cloud-covered atmospheres (Macintosh et al. 2015). The spectra show evidence for strong methane and water absorption (Macintosh et al. 2015); however, CH_4 is underabundant in comparison with chemical equilibrium, indicating that quenching is occurring and thus CO should also be abundant. Model-data comparisons favor $T_{\rm eff} = 700^{+50}_{-100}$ K, but the surface gravity is not well constrained (Macintosh et al. 2015). Because the planet is colder, contains more quenched CH_4, and receives a stronger UV flux at its ~14-au orbital distance (De Rosa et al. 2015) than HR 8799 b, photochemistry is expected to be more important on 51 Eri b, and indeed the recent independent photochemical modeling of Zahnle et al. (2016) demonstrates that this is the case.

Figure 15 shows the results for a 51 Eri b model with $T_{\rm eff} = 700$ K, $\log(g) = 3.5$ cgs (with assumed mass = $2M_J$, radius $\approx 1.25R_J$), $K_{\rm deep} = 2 \times 10^6$ cm^2 s^{-1}, and a solar metallicity, with a thermal structure derived from the radiative-convective equilibrium model described in Marley et al. (2012). We added an arbitrary 1000 K thermosphere to the top of this model, in an analogy with Jupiter, but we found that the presence or absence of such a thermosphere has little effect on the results. Note that this particular $K_{\rm deep}$ value was selected because it produces a quenched CH_4 abundance consistent with the absorption depths seen the Macintosh et al. (2015) spectra. Because the stratospheric temperature drops below 250 K, water recycling is relatively inefficient (see discussion in Section 3.1 and in Zahnle et al. 2016), and as the H_2O becomes depleted due to photolysis, the production of CO_2 through $CO + OH \rightarrow CO_2 + H$ proceeds prolifically. Carbon dioxide then becomes a major constituent on 51 Eri b at column abundances much greater than on HR 8799 b. The inefficiency of water recycling also leads to greater abundances of other oxidized products such as O_2, NO, H_2CO, CH_3OH, and HNCO. The high UV flux, large quenched CH_4 abundance, and cold stratosphere also allow greater production of complex hydrocarbons than in the HR 8799 b models, but again, none of the species in our models become abundant enough to condense to form hazes. The predicted NH_3 abundance is significantly smaller than expected from chemical equilibrium due to the N_2-NH_3 quenching, and since N_2 is more stable chemically, the photochemical production of nitrogen species is limited by this relatively low NH_3 abundance. HCN is the dominant product of the coupled carbon–nitrogen photochemistry, but with the low derived $K_{\rm deep}$ for this model, quenching is less important in controlling

the final HCN abundance than photochemistry. The column abundances of several species from this model are provided in Table 2.

Although the disequilibrium composition of warmer young Jupiters like HR 8799 b resembles that of close-in hot Jupiters, cooler young Jupiters like 51 Eri b are in a unique regime of their own. Both photochemistry and quenching sculpt the composition, and the cooler stratospheric temperatures allow a variety of photochemical products to thrive. Carbon dioxide becomes one of the dominant atmospheric constituents, in a process that is unique to cooler young Jupiters and brown dwarfs. For stratospheres warmer than ~250 K, the OH released from H_2O photolysis can still efficiently react with H_2 to recycle the water, but this reaction slows to a trickle at low temperatures. A large percentage of the upper-stratospheric oxygen then is removed from CO and H_2O and ends up in CO_2. This process does not occur on hot Jupiters because the temperatures are too high and the water and CO are efficiently recycled, and it does not occur on solar-system giant planets because overall stratospheric oxygen abundances are too low as a result of water condensation in the troposphere and small external oxygen influx rates due to interplanetary dust, cometary impacts, and satellite and ring debris (e.g., Moses et al. 2004).

Based on the column abundances predicted in this model (Table 2), CO_2 should be readily observable on 51 Eri b in the 4.2–4.3 μm and ~15 μm regions, and perhaps even near 2.7–2.8 μm. Carbon monoxide should also be observable at 2.3–2.4 μm (given sufficient spectral resolution) and at 4.5–4.9 μm. Ammonia absorption is potentially detectable in bands near ~1.5, 2, 3, and 6.15 μm if the lines can be disentangled from other absorbers and if the photosphere extends deep enough (i.e., is not obscured by high clouds), and NH_3 should be more readily detectable in the 9–11 μm region. Figure 16 demonstrates that photochemical models with relatively large quenched methane abundances can reproduce the GPI spectra.

Our photochemical model results for 51 Eri b are qualitatively similar to those of Zahnle et al. (2016), who use a different model, with a different numerical integrator, a different list of chemical species, different reaction rates and UV cross sections, different eddy diffusion coefficient profiles, and different assumptions about the stellar flux. Comparisons between the two models therefore give some sense of the robustness of the theoretical predictions regarding the photochemical products. The key quench reactions have different rate coefficients in the two models, so each model predicts slightly different quenched mixing ratios for any given $K_{\rm deep}$,
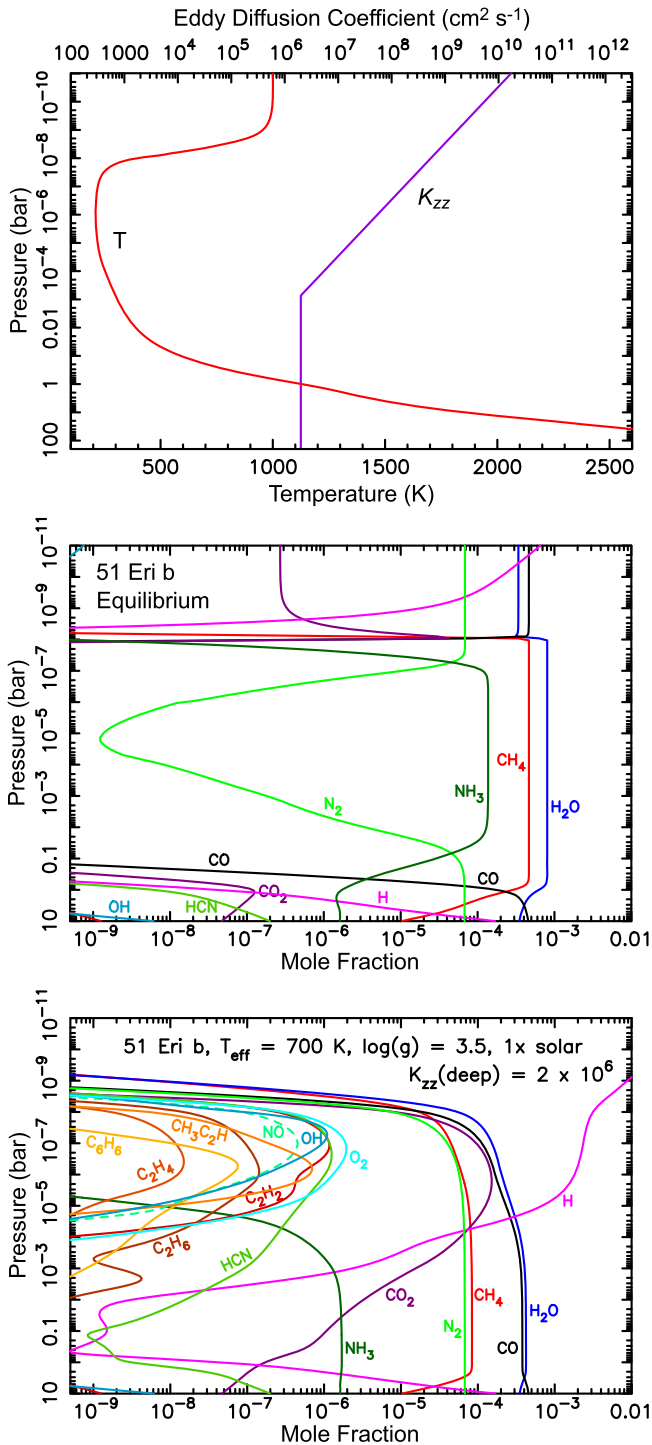
Figure 15. Chemical model for 51 Eri b assuming $T_{eff} = 700$ K, $\log(g) = 3.5$ cgs, mass = $2M_J$, and solar metallicity. (Top) The temperature profile (red curve, bottom axis) from the radiative-convective equilibrium model of Marley et al. (2012) assuming the above bulk constraints, and the eddy diffusion coefficient profile (purple curve, top axis) adopted in the photochemical model; (Middle) the predicted thermochemical equilibrium mixing-ratio profiles for the major oxygen, carbon, and nitrogen species, as labeled, for the assumed pressure–temperature profile; (Bottom) mixing-ratio profiles predicted from our thermo/photochemical kinetics and transport model for the above thermal structure, K_{zz} profile, and assumed bulk elemental composition.

Table 2
Column Abundances for 51 Eri b Models

| Species	Column Abundance Above 10 mbar (cm^{-2})	Column Abundance Above 100 mbar (cm^{-2})	Column Abundance Above 1 bar (cm^{-2})
CH$_4$	6.8×10^{19}	6.8×10^{20}	6.8×10^{21}
C$_2$H$_2$	4.8×10^{14}	4.8×10^{14}	4.8×10^{14}
C$_2$H$_6$	1.6×10^{15}	3.6×10^{15}	1.2×10^{16}
C$_3$H$_4$	1.5×10^{14}	1.5×10^{14}	1.5×10^{14}
C$_6$H$_6$	3.7×10^{14}	7.9×10^{14}	1.4×10^{15}
O$_2$	8.2×10^{14}	8.2×10^{14}	8.2×10^{14}
H$_2$O	3.4×10^{20}	3.4×10^{21}	3.4×10^{22}
CO	3.0×10^{20}	3.1×10^{21}	3.1×10^{22}
CO$_2$	6.9×10^{18}	1.8×10^{19}	5.0×10^{19}
H$_2$CO	2.4×10^{13}	1.8×10^{14}	7.4×10^{15}
CH$_3$OH	6.8×10^{13}	8.7×10^{14}	2.4×10^{15}
NH$_2$	7.5×10^{14}	7.5×10^{14}	7.6×10^{14}
NH$_3$	1.2×10^{18}	1.3×10^{19}	1.4×10^{20}
HCN	3.6×10^{16}	6.5×10^{16}	2.0×10^{17}
HC$_3$N	3.6×10^{14}	4.9×10^{14}	4.9×10^{14}
NO	5.1×10^{13}	5.1×10^{13}	5.1×10^{13}

Note. Model assumes $\log(g) = 3.5$ cgs.
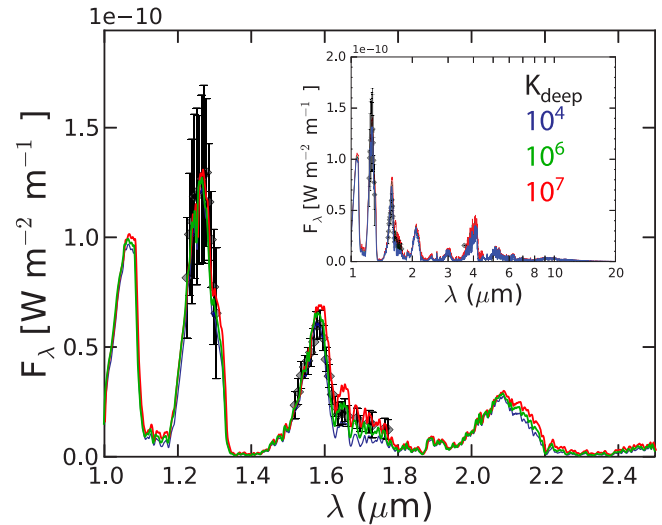
Figure 16. The 51 Eri b GPI observations of Macintosh et al. (2015) (gray/black data points with error bars), in comparison with synthetic spectra from photochemical models that assume $T_{eff} = 700$ K, $g = 3500$ cm s^{-2}, a solar metallicity, $Rv0.8R_J$, and $K_{deep} = 10^4$ (blue), 10^4 (green), or 10^7 cm^2 s^{-1} (red). Lower K_{deep} values lead to larger quenched CH$_4$ abundances and greater absorption in the long-wavelength side of the H band. The inset shows an expanded wavelength range. As indicated by Macintosh et al. (2015), we also find that we need to invoke partial cloud cover in order to reproduce the near-infrared observations. For this particular analysis, we combined the spectrum of a cloud-free planet with one covered by a uniform global cloud, such that the "cloud fraction" was 30%. The cloudy model assumed a uniform gray absorbing cloud with a base at ~10 bar (representing Mg-silicates) and an optical depth of 1.76 between 0.1 and 1000 mbar (e.g., from Na$_2$S clouds or photochemical haze). The planet was assumed to be 29.4 pc from Earth.

but these differences are relatively minor (i.e., within a factor of ~2 for CH$_4$). Both models predict strong photochemical production of CO$_2$ when the stratospheric temperatures fall

below ~250 K, and both models predict that a variety of complex hydocarbons will be produced photochemically in the middle and upper stratosphere of 51 Eri b. The Zahnle et al. (2016) model includes sulfur chemistry, while the model presented here does not, and the list of complex hydrocarbon and nitrogen species and reactions is more extensive in the model here than in Zahnle et al. (2016). Because the nominal

Zahnle et al. ([2016](#)) model does not contain as effective loss processes for some hydrocarbons such as C_4H_2, their model predicts greater abundances of these hydrocarbons, and Zahnle et al. ([2016](#)) presume that these hydrocarbons go on to inevitably form PAHs and organic hazes, as an upper limit to possible photochemical haze formation. The hydrocarbon chemistry presented here, which includes more C_4H_x, C_5H_x, and C_6H_x hydrocarbons (including benzene) but not PAHs or heavier hydrocarbons, predicts more efficient conversion of the complex hydrocarbons back into simple hydrocarbons, CO, CO_2, and HCN, so the effectiveness of organic haze formation on 51 Eri b has not been demonstrated. Neither model includes ion chemistry or neutral-chemistry pathways to larger organic molecules. The model here predicts a larger CO_2 abundance than is obtained in Zahnle et al. ([2016](#)), for otherwise identical conditions. This result seems to stem from the presence of sulfur species in the Zahnle et al. model, where H_2S is readily destroyed by long-wavelength UV radiation, with the sulfur ending up in S_8 and oxidized species, and the excess H released in the process helping to convert some of the CO_2 back to CO.

4. DISCUSSION

4.1. Implications of Disequilibrium CO_2

Our photochemical models for generic directly imaged planets and the specific young Jupiters HR 8799 b and 51 Eri b indicate that CO_2 is a major disequilibrium product on young Jupiters that is affected by both quenching and photochemistry. The CO_2 abundance can increase significantly when stratospheric temperatures drop below $\sim$250 K, when metallicities are larger than solar, and when the eddy diffusion coefficients in the troposphere and lower stratosphere are relatively small (e.g., $K_{zz} < 10^7$ cm^2 s^{-1}). The CO_2 produced by disequilibrium processes is likely to affect the planet's emission spectrum, especially in the $\sim$4.3- and 15 μm regions. Detection could help constrain the planet's atmospheric metallicity, especially if K_{zz} at the quench point has already been constrained from the observed relative abundance of CH_4 and CO.

Quenching (and potentially photochemistry, depending on local UV sources) will affect the CO_2 abundance on brown dwarfs, as well. Brown dwarfs with lower T_{eff} and colder stratospheres are expected to have more CO_2 simply as a result of quenching, and the CO_2 abundance can further be enhanced by photochemistry if there is a UV background sufficient to cause H_2O photolysis. Perhaps galactic cosmic rays could also contribute to CO_2 production if that resulting chemistry leads to a similar destruction pathway for H_2O, and if OH + H_2 $\rightarrow$ H_2O + H is relatively inefficient (i.e., for cooler stratospheres). If photochemistry or cosmic-ray chemistry can lead to CO_2 production on brown dwarfs, then that could explain the trends seen in the AKARI data of Yamamura et al. ([2010](#)), who find that the CO_2 absorption band at $\sim$4.2–4.3 μm is enhanced tremendously in cooler late L and T dwarfs.

4.2. Implications of Disequilibrium HCN

Hydrogen cyanide is the second most important product of disequilibrium chemistry on young Jupiters. The HCN abundance is increased when the tropospheric K_{deep} is large and the lower stratospheric K_{zz} is small (i.e., a stagnant lower stratosphere overlying a convective troposphere). The strong HCN band near 3 μm may be detectable on young Jupiters if high clouds do not fully obscure the upper troposphere, although a relatively high spectral resolution may be needed to disentangle the HCN lines from other absorbers such as CH_4. A source of atomic H from H_2S and PH_3 at depth (not included in this model) could lead to increased HCN abundances by attacking CH_4 and NH_3 to produce CH_3 and NH_2, augmenting coupled carbon–nitrogen photochemistry through CH_3NH_2 pathways such as scheme (6) above and others described more fully in Moses et al. ([2010](#), [2011](#)).

4.3. Implications for Hazes

Our neutral carbon, oxygen, and nitrogen photochemistry described here does not lead to the production of organic hazes in our young-Jupiter models. Some complex organics are produced in the models, but the abundances are not large enough in these generally warm stratospheres to lead to supersaturations. Note that the complex organics in our directly imaged planet models are less abundant than on Jupiter and Saturn, and yet the stratospheric hazes on our solar-system giant planets are not optically thick when the refractory organics such as C_4H_2, C_4H_{10} and C_6H_6 become supersaturated and condense (e.g., Moses et al. [2004](#); West et al. [2004](#)). Therefore, optically thick hydrocarbon hazes on young Jupiters might not be expected. However, ion chemistry in the auroral regions of Jupiter and Saturn seems to be more effective at producing PAHs and other complex hydrocarbons that then condense in the high-latitude stratosphere to form thicker "polar hoods" of aerosols (e.g., Pryor & Hord [1991](#); Wong et al. [2000](#), [2003](#); Friedson et al. [2002](#)).

Ion chemistry on young Jupiters may therefore enhance the production of complex hydrocarbons and eventual hazes, but even in the presence of ionization, optically thick haze formation is not guaranteed. For example, solar ionization of hydrocarbons is effective at low-to-mid latitudes on Jupiter and Saturn (e.g., Kim & Fox [1994](#); Kim et al. [2014](#)), but optically thick stratospheric photochemical hazes do not result from this process. Several Titan laboratory simulations demonstrate that PAH formation is favored when molecular nitrogen is present and is ionized (e.g., Imanaka & Smith [2007](#)). Whether this rich Titan-like ion chemistry can still occur in warmer H_2-dominated situations, where the CH_4 homopause limits altitude range over which the ion chemistry is effective and for which O and OH are present to potentially short-circuit the process by oxidizing the carbon and sending it preferentially to CO and CO_2, remains to be seen. Laboratory investigations similar to those of Imanaka & Smith [2009](#); Sciamma-O'Brien et al. [2010](#); Peng et al. [2013](#), and Hörst & Tolbert ([2014](#)) but that are specifically designed for stratospheric conditions on young Jupiters would further our understanding of the likelihood of organic photochemical hazes.

Other possibilities for clouds and hazes on young Jupiters include the standard equilibrium cloud sequence (e.g., Morley et al. [2012](#); Marley et al. [2013](#)), for which magnesium-silicate clouds might affect spectra if they are vertically thick, and for which Na_2S clouds are likely to reside within the photospheres of many young Jupiters (see Figure [1](#)). Zahnle et al. ([2016](#)) identify elemental sulfur as another intriguing possible photochemical haze that is particularly likely when the stratosphere is relatively cold and well irradiated. Hydrogen sulfide is chemically fragile, and although the kinetics of sulfur species is not well determined for relevant atmospheric conditions, the formation of S_8 molecules as described by Zahnle et al. ([2016](#)) seems a likely possibility. Zahnle et al.

(2016) find that sulfur chemistry would destroy all photospheric H_2S for a 51 Eri b planet at an orbital distance of $\lesssim$ 600 au. Phosphine (PH_3) is also a chemically fragile molecule, and the phosphorus may end up in elemental phosphorus or other relatively refractory photochemical species that could eventually form hazes. The identity of the clouds that seem to affect the spectra of young Jupiters is therefore unclear, but there are many candidate materials, including photochemical hazes.

4.4. Implications for JWST and WFIRST

The *JWST* will have the capability of obtaining high-contrast ($\geqslant 10^{-7}$) images of young giant planets (Beichman et al. 2010; Clampin 2011), with well-separated ones ($3''$–$10''$) being amenable to spectroscopic characterization. The Near Infrared Camera (NIRCam), Mid-Infrared Instrument (MIRI), and Near-InfraRed Imager and Slitless Spectrograph (NIRISS) all have imaging modes, with MIRI and NIRCam having coronagraph options (e.g., Krist et al. 2007; Boccaletti et al. 2015; Debes et al. 2015) and NIRISS having an Aperture Masking Interferometry (AMI) mode (Artigau et al. 2014). Additionally, the *JWST* Near Infrared Spectrograph (NIRSpec) and MIRI instruments both have Integral Field Units (IFUs) (Arribas et al. 2007; Wells et al. 2015) that will allow for medium to high resolution ($R \sim$ 1000–3000) spectra of planets with angular separations greater than $3''$. Collectively these instruments can provide high-sensitivity photometry and spectroscopy of giant planets orbiting at a variety of separations ($0''.1$–$10''$) from their host stars, over the wavelength range $\sim$0.6–28 μm (see the review of Beichman et al. 2010). *JWST* will therefore provide the opportunity for detecting the excess CO_2 absorption we predict here near $\sim$4.3 μm (see Figure 10) and $\sim$15 μm, as well as provide better constraints on the quenched methane abundance from absorption in the 3.3- and 7.7 μm bands, quenched NH_3 from the 10–11 μm band, signatures of photochemically produced species such as HCN (near $\sim$3, 7, and 14 μm), C_2H_2 (at 13.6 μm), and C_2H_6 (near 12.2 μm).

In the next decade, NASA's Wide Field Infrared Survey Telescope (WFIRST), equipped with an optical (0.4–0.95 μm) Coronagraphic Instrument (CGI), will obtain photometry and spectra for extrasolar planets with contrasts as low as 10^{-10} and angular separations between $0''.1$ and $0''.5$ (Traub et al. 2016). The WFIRST CGI prime survey will target a number of planets detected via radial velocity both photometrically (0.4–0.95 μm) and spectroscopically (0.6–0.95 μm). These planets will be relatively cool, mature giant planets orbiting closer to their stars than Jupiter. Many of these planets will be warm enough to lack ammonia, hydrogen sulfide, and in some cases, water clouds (Marley et al. 2014). Thus their predicted photospheric equilibrium chemistry is comparable to the directly imaged planets studied here, although their deep atmospheres will be colder. Methane is likely the dominant form of carbon in the atmospheres of these planets, and although detailed predictions for the photochemistry of such worlds awaits future studies, the implications of our models presented here point to a likely rich photochemistry. Preliminary investigations (Sharp et al. 2004) suggest that the older Jupiters with neither water nor ammonia trapped in tropospheric clouds (i.e., the "Class III" planets in the terminology of, Sudarsky et al. 2003) will have stratospheric chemistry similar to what is described for our young-Jupiter

models. Sharp et al. (2004) find that hydrocarbon and nitrile photochemistry is even more prevalent on "Class II" planets, for which water condenses in the troposphere but ammonia does not (Sudarsky et al. 2003), leading to high production rates for HCN, CH_3CN, other nitriles, and complex hydrocarbons. Coupled C_2H_2-NH_3 photochemistry will likely produce high-molecular-weight organo-nitrogen compounds (Moses et al. 2010) and PAHs. Photochemical production of hazes will likely be important, which can sculpt the ultraviolet and blue reflection spectra (e.g., Griffith et al. 1998), as on our own solar-system giant planets, thereby affecting the reflection photometry or signatures observed by WFIRST.

5. CONCLUSIONS

Our modeling of directly imaged exoplanets indicates that the atmospheric composition of these young Jupiters is expected to be far from chemical equilibrium, confirming the results of previous studies that indicate CH_4 and CO quenching is occurring on these planets (e.g., Bowler et al. 2010; Hinz et al. 2010; Janson et al. 2010, 2013; Barman et al. 2011a, 2011b, 2015; Galicher et al. 2011; Marley et al. 2012; Skemer et al. 2012, 2014; Currie et al. 2014; Ingraham et al. 2014; Zahnle & Marley 2014). Transport-induced quenching will cause CO, and not CH_4, to be the dominant carbon constituent on most lower-gravity young Jupiters with $T_{\text{eff}} \geqslant 600$ K, for all reasonable estimates of the strength of deep-atmospheric convection. This conclusion is inevitable. The first line of attack for interpreting young-Jupiter spectra should therefore always be models that include quenching. Photochemistry can also play a significant role in young-Jupiter atmospheres, especially on cooler planets that receive strong ultraviolet irradiation from their host stars.

Rapid transport in the deep atmosphere also leads to quenching of H_2O at the same point as the quenching of CO and CH_4. This effect does not appear to be as widely realized as the CH_4–CO quenching phenomenon, but it is important, as the quenching can occur in a region where the equilibrium H_2O mixing ratio is increasing with altitude, with quenching then causing a lower-than-expected H_2O abundance on young Jupiters. In this situation, the oxygen is preferentially tied up in quenched CO rather than H_2O, and the water mixing ratio can be a factor of a few lower than equilibrium predictions. Water is the dominant infrared opacity source on young Jupiters, and the fact that quenching can alter the expected abundance can in turn affect the predicted thermal structure, cooling history, spectral energy distribution, and inferred C/O ratio of these planets (the latter due to the fact that the CO abundance is typically difficult to constrain precisely). Models that consider the thermal evolution of giant planets or that predict the current thermal structure of young Jupiters should take the quenching of H_2O into account, although this factor is not likely to have as large an impact as clouds or initial conditions.

Quenching will also affect the relative abundances of NH_3 and N_2, favoring N_2 rather than NH_3 at the quench point. Although NH_3 is not expected to be the dominant nitrogen-bearing constituent, the quenched ammonia abundance may still be observable on young Jupiters if the photosphere extends into the upper troposphere and is not obscured by clouds. The quenched NH_3 mixing ratio increases as T_{eff} decreases.

Other potentially observable constituents that are expected to be negligible in equilibrium models but that are affected by

disequilibrium chemical processes include CO_2 and HCN. These molecules are affected by both quenching and photochemistry. The quenching process leads to increases in the HCN abundance when deep atmospheric mixing is strong, while increases in CO_2 are favored when deep atmospheric mixing is weak. Photochemical production of both HCN and CO_2 is more important for weak lower-stratospheric mixing and strong UV irradiation. Effective temperatures of 900–1400 K favor larger HCN column abundances, whereas the CO_2 column abundance increases significantly for lower T_{eff}, and specifically for low stratospheric temperatures $T \lesssim 250$ K. When stratospheric temperatures are low, the reaction $OH + H_2 \rightarrow H_2O + H$ becomes ineffective, and $OH + CO \rightarrow CO_2 + H$ can compete (see also Zahnle et al. 2016), depleting the upper stratospheric H_2O and CO, and significantly increasing the column abundance of photochemically produced CO_2. On cooler planets like 51 Eri b, the CO_2 peak mixing ratio can even exceed that of CH_4 and rivals that of CO and H_2O in the upper stratosphere. Carbon dioxide is likely to be observable on all young Jupiters with moderate-to-low atmospheric mixing, but will be especially important on cooler planets. Hydrogen cyanide is less likely to be observable on young Jupiters, but it may be detectable in the $\sim 3\,\mu$m band given favorable atmospheric conditions (including the absence of high clouds) and sufficient spectral resolution to disentangle the lines from other nearby absorbers.

Complex hydrocarbons also form photochemically on young Jupiters, but the generally warm stratospheric temperatures and large H abundance make them less stable than on the giant planets in our solar system. Oxidation of the carbon to form CO and CO_2 also competes effectively, unlike on our own giant planets. It is unlikely that hydrocarbons produced from neutral photochemistry will be observable on young Jupiters. Note that the models presented here include only H-, C-, O-, and N-bearing species. Ion chemistry is not included, nor is the neutral photochemistry of other volatiles like sulfur and phosphorus. As shown by Zahnle et al. (2016), sulfur chemistry can alter some of the predictions regarding the abundances of C-, N-, and O- species. Although organic hazes do not form from the neutral chemistry considered here, ion chemistry may augment the production of refractory organics, as on Titan and in the auroral regions of Jupiter (e.g., Wong et al. 2000; Vuitton et al. 2007; Waite et al. 2007). Future laboratory and theoretical modeling should focus on this possibility. Laboratory studies that investigate the kinetics of C_3H_2 and C_3H_3 reactions with other hydrocarbon radicals and molecules would aid exoplanet photochemistry studies. Other possible photochemically produced hazes include elemental sulfur (Zahnle et al. 2016), elemental phosphorus or other refractory phosphorus species, and refractory products from coupled C_2H_2–NH_3 chemistry (e.g., Keane et al. 1996; Ferris & Ishikawa 1988; Moses et al. 2010).

Detection and abundance determinations for key molecules like CH_4, H_2O, CO, CO_2, and NH_3 can help constrain planetary properties and potentially break other modeling degeneracies. The CH_4 and NH_3 mixing ratios are strong indicators of the strength of deep atmospheric mixing, K_{deep}, as well as the planet's effective temperature, T_{eff}. Simultaneous measurements of the abundance of H_2O and CO can provide additional constraints on T_{eff}, surface gravity, and metallicity. The CO_2 abundance is very sensitive to metallicity (e.g., Lodders & Fegley 2002; Moses et al. 2013a), and can also become quite large for low T_{eff}, low stratospheric K_{zz}, and high UV irradiance.

The disequilibrium composition of warmer young Jupiters (i.e., $T_{eff} \gtrsim 900$ K), such as HR 8799 b, resembles that of close-in transiting giant planets. Transport-induced quenching is the dominant process driving the atmospheres out of equilibrium, and the stratospheres are too warm to allow many of the photochemical products to survive, other than molecules with strong bonds like C_2H_2 and HCN. However, cooler young Jupiters ($T_{eff} \lesssim 700$ K) like 51 Eri b can have a rich and interesting photochemistry that differs distinctly from that of either hot Jupiters or the cold giant planets in our solar system. The quenched abundances of photochemically active CH_4 and NH_3 tend to be greater for lower T_{eff}, and hydrocarbon photochemical products survive more readily when stratospheric temperatures are low. Oxidation of the carbon and nitrogen species can also proceed much more effectively when stratospheric temperatures are low (due to a reduction in efficiency of H_2O recycling), leading to oxidized products like NO, O_2, and especially CO_2. Carbon dioxide is likely to be a major absorber on cooler young Jupiters.

Cooler directly imaged giant planets that receive moderate-to-high UV flux from their host stars fall into a unique and interesting chemical regime that is controlled by both transport-induced quenching and an active, rich photochemistry. This chemical regime has no representation in our own solar system because the terrestrial planets have very different atmospheric compositions and the colder giant planets have key oxygen and nitrogen species tied up in condensates at depth, so that coupled nitrogen-carbon, oxygen-carbon, and nitrogen-oxygen photochemistry is suppressed. The simultaneous presence of H_2O, CO, CH_4, N_2, and NH_3 on cooler young Jupiters leads to complex photochemical interactions with both oxidized and reduced products being stable, and small amounts of high-molecular-weight pre-biotic molecules being able to form and survive. With dedicated ground-based campaigns ramping up their search for young Jupiters (e.g., Macintosh et al. 2015; Tamura 2016; Vigan et al. 2016), and missions such as *JWST*, GAIA, and WFIRST gearing up or being planned, we look forward to many future reports of the atmospheric composition of directly imaged giant planets.

REFERENCES

Agúndez, M., Parmentier, V., Venot, O., Hersant, F., & Selsis, F. 2014a, A&A, 564, A73

Agúndez, M., Venot, O., Selsis, F., & Iro, N. 2014b, ApJ, 781, 68

Allard, F., Hauschildt, P. H., Alexander, D. R., Tamanai, A., & Schweitzer, A. 2001, ApJ, 556, 357

Allen, M., Yung, Y. L., & Waters, J. W. 1981, JGR, 86, 3617

Arribas, S., Ferruit, P., Jakobsen, P., et al. 2007, in Science Perspectives for 3D Spectroscopy, ed. M. Kissler-Patig, J. R. Walsh, & M. M. Roth (Berlin: Springer), 21

Artigau, É., Sivaramakrishnan, A., Greenbaum, A. Z., et al. 2014, Proc. SPIE, 9143, 914340

Atkinson, D. B., & Hudgens, J. 1999, JPCA, 103, 4242

Atreya, S. K., Donahue, T. M., Nagy, A. F., Waite, J. H., Jr., & McConnell, J. C. 1984, in Saturn, ed. T. Gehrels & M. S. Matthews (Tucson, AZ: Univ. Arizona Press), 239

Atreya, S. K., & Romani, P. N. 1985, in Recent Advances in Planetary Meteorology, ed. G. E. Hunt (Cambridge: Cambridge Univ. Press)

Bailey, J. 2014, PASA, 31, e043

Barman, T. S., Konopacky, Q. M., Macintosh, B., & Marois, C. 2015, ApJ, 804, 61

Barman, T. S., Macintosh, B., Konopacky, Q. M., & Marois, C. 2011a, ApJ, 733, 65

Barman, T. S., Macintosh, B., Konopacky, Q. M., & Marois, C. 2011b, ApJL, 735, L39

Baudino, J.-L., Bézard, B., Boccaletti, A., et al. 2015, A&A, 582, A83

Baulch, D. L., Bowman, C. T., Cobos, C. J., et al. 2005, JPCRD, 34, 757

Beichman, C. A., Krist, J., Trauger, J. T., et al. 2010, PASP, 122, 162

Benneke, B. 2015, arXiv:1504.07655

Bézard, B., Lellouch, E., Strobel, D., Maillard, J.-P., & Drossart, P. 2002, Icar, 159, 95

Boccaletti, A., Lagage, P.-O., Baudoz, P., et al. 2015, PASP, 127, 633

Bonnefoy, M., Boccaletti, A., Lagrange, A.-M., et al. 2013, A&A, 555, A107

Bonnefoy, M., Zurlo, A., Baudino, J. L., et al. 2016, A&A, 587, A58

Bowler, B. P. 2016, PASP, 128, 102001

Bowler, B. P., Liu, M. C., Dupuy, T. J., & Cushing, M. C. 2010, ApJ, 723, 850

Brasseur, G. P., Orlando, J. J., & Tyndall, G. S. 1999, Atmospheric Chemistry and Global Change (New York: Oxford Univ. Press)

Burrows, A., Sudarsky, D., & Lunine, J. I. 2003, ApJ, 596, 587

Castelli, F., & Kurucz, R. L. 2004, arXiv:astro-ph/0405087

Chilcote, J., Barman, T., Fitzgerald, M. P., et al. 2015, ApJL, 798, L3

Clampin, M. 2011, in Proc. IAU Symp. 276, The Astrophysics of Planetary Systems: Formation, Structure, and Dynamical Evolution, ed. A. Sozzetti, M. G. Lattanzi, & A. P. Boss (Cambridge: Cambridge Univ. Press), 335

Crossfield, I. J. M. 2015, PASP, 127, 941

Currie, T., Burrows, A., Girard, J. H., et al. 2014, ApJ, 795, 133

Currie, T., Burrows, A., Itoh, Y., et al. 2011, ApJ, 729, 128

De Rosa, R. J., Nielsen, E. L., Blunt, S. C., et al. 2015, ApJL, 814, L3

Dean, A. M., Chou, M.-S., & Stern, D. 1984, Int. J. Chem. Kinet., 16, 633

Debes, J. H., Ygouf, M., Choquet, E., et al. 2015, arXiv:1511.06277

Dobrijevic, M., Cavalié, T., Hébrard, E., et al. 2010, P&SS, 58, 1555

Fahr, A., & Nayak, A. 2000, Int. J. Chem. Kinet., 32, 118

Fegley, B., Jr., & Lodders, K. 1994, Icar, 110, 117

Ferris, J. P., & Ishikawa, Y. 1988, JAChS, 110, 4306

Fortney, J. J., Marley, M. S., Saumon, D., & Lodders, K. 2008b, ApJ, 683, 1104

Fouchet, T., Moses, J. I., & Conrath, B. J. 2009, in Saturn from Cassini-Huygens, ed. M. K. Dougherty, L. W. Esposito, & S. M. Krimigis (Berlin: Springer), 83

Freytag, B., Allard, F., Ludwig, H.-G., Homeier, D., & Steffen, M. 2010, A&A, 513, A19

Friedson, A. J., Wong, A.-S., & Yung, Y. L. 2002, Icar, 158, 389

Galicher, R., Marois, C., Macintosh, B., Barman, T., & Konopacky, Q. 2011, ApJL, 739, L41

Gordon, S., & McBride, B. J. 1994, NASA Reference Publ., 1311

Grevesse, N., Asplund, M., & Sauval, A. 2007, SSRv, 130, 105

Griffith, C. A., & Yelle, R. V. 1999, ApJL, 519, L85

Griffith, C. A., Yelle, R. V., & Marley, M. S. 1998, Sci, 282, 2063

Hauschildt, P. H., Baron, E., & Allard, F. 1997, ApJ, 483, 390

Heap, S. R., & Lindler, D. 2011, in ASP Conf. Ser. 448, 16th Cambridge Workshop on Cool Stars, Stellar Systems, and the Sun, ed. C. Johns-Krull, M. K. Browning, & A. A. West (San Francisco, CA: ASP), 887

Hébrard, E., Dobrijevic, M., Loison, J. C., et al. 2013, A&A, 552, A132

Heng, K., Lyons, J. R., & Tsai, S.-M. 2016, ApJ, 96, 96

Hidaka, Y., Oki, Y., & Kawano, H. 1989, JPhCh, 93, 7134

Hinz, P. M., Rodigas, T. J., Kenworthy, M. A., et al. 2010, ApJ, 716, 417

Hörst, S. M., & Tolbert, M. A. 2014, ApJ, 781, 53

Hörst, S. M., Yelle, R. V., Buch, A., et al. 2012, AsBio, 12, 809

Hu, R., & Seager, S. 2014, ApJ, 784, 63

Hubeny, I., & Burrows, A. 2007, ApJ, 669, 1248

Imanaka, H., & Smith, M. A. 2007, GeoRL, 34, L02204

Imanaka, H., & Smith, M. A. 2009, JPCA, 113, 11187

Ingraham, P., Marley, M. S., Saumon, D., et al. 2014, ApJL, 794, L15

Janson, M., Bergfors, C., Goto, M., Brandner, W., & Lafrenière, D. 2010, ApJL, 710, L35

Janson, M., Brandt, T. D., Kuzuhara, M., et al. 2013, ApJL, 778, L4

Jasper, A. W., Klippenstein, S. J., Harding, L. B., & Ruscic, B. 2007, JPCA, 111, 3932

Kaye, J. A., & Strobel, D. F. 1983, Icar, 55, 399

Keane, T. C., Yuan, F., & Ferris, J. P. 1996, Icar, 122, 205

Kim, Y. H., & Fox, J. L. 1994, Icar, 112, 310

Kim, Y. H., Fox, J. L., Black, J. H., & Moses, J. I. 2014, JGR, 119, 384

Klippenstein, S. J., Harding, L. B., Ruscic, B., et al. 2009, JPCA, 113, 10241

Knyazev, V. D., & Slagle, I. R. 2001, JPCA, 105, 3196

Konnov, A. A., & De Ruyck, J. 2000, CST, 152, 23

Konopacky, Q. M., Barman, T. S., Macintosh, B. A., & Marois, C. 2013, Sci, 339, 1398

Kopparapu, R. k., Kasting, J. F., & Zahnle, K. J. 2012, ApJ, 745, 77

Krist, J. E., Beichman, C. A., Trauger, J. T., et al. 2007, Proc. SPIE, 6693, 66930H

Landsman, W., & Simon, T. 1993, ApJ, 408, 305

Lavvas, P., Koskinen, T., & Yelle, R. V. 2014, ApJ, 796, 15

Lee, J.-M., Heng, K., & Irwin, P. G. J. 2013, ApJ, 778, 97

Lendvay, G., Bérces, T., & Márta, F. 1997, JPCA, 101, 1588

Lewis, J. S., & Fegley, M. B., Jr. 1984, SSRv, 39, 163

Liang, M.-C., Parkinson, C. D., Lee, A. Y.-T., Yung, Y. L., & Seager, S. 2003, ApJL, 596, L247

Lindzen, R. S. 1981, JGR, 86, 9707

Line, M. R., Fortney, J. J., Marley, M. S., & Sorahana, S. 2014, ApJ, 793, 33

Line, M. R., Teske, J., Burningham, B., Fortney, J. J., & Marley, M. S. 2015, ApJ, 807, 183

Line, M. R., Vasisht, G., Chen, P., Angerhausen, D., & Yung, Y. L. 2011, ApJ, 738, 32

Line, M. R., Wolf, A. S., Zhang, X., et al. 2013, ApJ, 775, 137

Lodders, K. 2010, in Formation and Evolution of Exoplanets, ed. R. Barnes (Berlin: Wiley), 157

Lodders, K., & Fegley, B. 2002, Icar, 155, 393

Macintosh, B., Graham, J. R., Barman, T., et al. 2015, Sci, 350, 64

Madhusudhan, N., Agúndez, M., Moses, J. I., & Hu, Y. 2016, SSRv, in press doi:10.1007/s11214-016-0254-3

Madhusudhan, N., Burrows, A., & Currie, T. 2011, ApJ, 737, 34

Madhusudhan, N., Knutson, H., Fortney, J. J., & Barman, T. 2014, in Protostars and Planets VI, ed. H. Beuther et al. (Tucson, AZ: Univ. Arizona Press), 739

Maire, A.-L., Skemer, A. J., Hinz, P. M., et al. 2015, A&A, 576, A133

Marley, M., Lupu, R., Lewis, N., et al. 2014, arXiv:1412.8440

Marley, M. S., Ackerman, A. S., Cuzzi, J. N., & Kitzmann, D. 2013, in Comparative Climatology of Terrestrial Planets, ed. S. J. Mackwell et al. (Tucson, AZ: Univ. Arizona Press), 367

Marley, M. S., Fortney, J., Seager, S., & Barman, T. 2007, in Protostars and Planets V, ed. B. Reipurth, D. Hewitt, & K. Keil (Tucson, AZ: Univ. Arizona Press), 733

Marley, M. S., Gelino, C., Stephens, D., Lunine, J. I., & Freedman, R. 1999, ApJ, 513, 879

Marley, M. S., Saumon, D., Cushing, M., et al. 2012, ApJ, 754, 135

Marley, M. S., Seager, S., Saumon, D., et al. 2002, ApJ, 568, 335

Marois, C., Macintosh, B., Barman, T., et al. 2008, Sci, 322, 1348

Marois, C., Zuckerman, B., Konopacky, Q. M., Macintosh, B., & Barman, T. 2010, Natur, 468, 1080

McKay, C. P., Pollack, J. B., & Courtin, R. 1989, Icar, 80, 23

Miguel, Y., & Kaltenegger, L. 2014, ApJ, 780, 166

Miguel, Y., Kaltenegger, L., Linsky, J. L., & Rugheimer, S. 2015, MNRAS, 446, 345

Millar, T. J., Bennett, A., Rawlings, J. M. C., Brown, P. D., & Charnley, S. B. 1991, A&AS, 87, 585

Miller-Ricci Kempton, E., Zahnle, K., & Fortney, J. J. 2012, ApJ, 745, 3

Morley, C. V., Fortney, J. J., Kempton, E. M.-R., et al. 2013, ApJ, 775, 33

Morley, C. V., Fortney, J. J., Marley, M. S., et al. 2012, ApJ, 756, 172

Morzinski, K. M., Males, J. R., Skemer, A. J., et al. 2015, ApJ, 815, 108

Moses, J. I. 2014, RSPTA, 372, 20130073

Moses, J. I., Armstrong, E. S., Fletcher, L. N., et al. 2015, Icar, 261, 149

Moses, J. I., Bézard, B., Lellouch, E., et al. 2000, Icar, 143, 244

Moses, J. I., Fouchet, T., Bézard, B., et al. 2005, JGR, 110, E08001

Moses, J. I., Fouchet, T., Yelle, R. V., et al. 2004, in Jupiter. The Planet, Satellites and Magnetosphere, ed. F. Bagenal, T. E. Dowling, & W. B. McKinnon (Cambridge: Cambridge Univ. Press), 129

Moses, J. I., Line, M. R., Visscher, C., et al. 2013a, ApJ, 777, 34

Moses, J. I., Madhusudhan, N., Visscher, C., & Freedman, R. S. 2013b, ApJ, 763, 25

Moses, J. I., Rages, K., & Pollack, J. B. 1995, Icar, 113, 232

Moses, J. I., Visscher, C., Fortney, J. J., et al. 2011, ApJ, 737, 15

Moses, J. I., Visscher, C., Keane, T. C., & Sperier, A. 2010, FaDi, 147, 103

Nagy, A. F., Kliore, A. J., Mendillo, M., et al. 2009, in Saturn from Cassini-Huygens, ed. M. K. Dougherty, L. W. Esposito, & S. M. Krimigis (Dordrecht: Springer), 181

Norton, T. S., & Dryer, F. L. 1989, CST, 63, 107

Norton, T. S., & Dryer, F. L. 1990, Int. J. Chem. Kinet., 22, 219

Öberg, K. I., Murray-Clay, R., & Bergin, E. A. 2011, ApJL, 743, L16

Oppenheimer, B. R., Baranec, C., Beichman, C., et al. 2013, ApJ, 768, 24

Orton, G. S., Moses, J. I., Fletcher, L. N., et al. 2014, Icar, 243, 471

Parmentier, V., Showman, A. P., & Lian, Y. 2013, A&A, 558, A91

Patience, J., King, R. R., de Rosa, R. J., & Marois, C. 2010, A&A, 517, A76

Peng, Z., Gautier, T., Carrasco, N., et al. 2013, JGR, 118, 778

Prinn, R. G., & Barshay, S. S. 1977, Sci, 198, 1031

Pryor, W. R., & Hord, C. W. 1991, Icar, 91, 161

Rajan, A., Barman, T., Soummer, R., et al. 2015, ApJL, 809, L33

Rimmer, P. B., & Helling, C. 2016, ApJS, 224, 9

Rimmer, P. B., Helling, C., & Bilger, C. 2014, IJAsB, 13, 173

Romani, P. N., Bishop, J., Bezard, B., & Atreya, S. 1993, Icar, 106, 442

Sanz-Forcada, J., Micela, G., Ribas, I., et al. 2011, A&A, 532, A6

Saumon, D., & Marley, M. S. 2008, ApJ, 689, 1327

Sciamma-O'Brien, E., Carrasco, N., Szopa, C., Buch, A., & Cernogora, G. 2010, Icar, 209, 704

Sharp, A. G., Moses, J. I., Friedson, A. J., et al. 2004, LPSC, 35, 1142

Sims, I. R., Queffelec, J.-L., Travers, D., et al. 1993, CPL, 211, 461

Skemer, A. J., Hinz, P. M., Esposito, S., et al. 2012, ApJ, 753, 14

Skemer, A. J., Marley, M. S., Hinz, P. M., et al. 2014, ApJ, 792, 17

Smith, M. D. 1998, Icar, 132, 176

Snellen, I. A. G., Brandl, B. R., de Kok, R. J., et al. 2014, Natur, 509, 63

Spiegel, D. S., & Burrows, A. 2012, ApJ, 745, 174

Stone, P. H. 1976, in Jupiter, ed. T. Gehrels (Tucson, AZ: Univ. Arizona Press), 586

Strobel, D. F. 1981, JGR, 86, 9806

Strobel, D. F. 1983, IRPC, 3, 145

Sudarsky, D., Burrows, A., & Hubeny, I. 2003, ApJ, 588, 1121

Summers, M. E., & Strobel, D. F. 1989, ApJ, 346, 495

Tamura, M. 2016, PJAB, 92, 45

Traub, W. A., Breckinridge, J., Greene, T. P., et al. 2016, JATIS, 2, 011020

Venot, O., Fray, N., Bénilan, Y., et al. 2013, A&A, 551, A131

Venot, O., Hébrard, E., Agúndez, M., et al. 2012, A&A, 546, A43

Vigan, A., Bonnefoy, M., Ginski, C., et al. 2016, A&A, 587, A55

Visscher, C., & Moses, J. I. 2011, ApJ, 738, 72

Visscher, C., Moses, J. I., & Saslow, S. A. 2010b, Icar, 209, 602

Vuitton, V., Yelle, R. V., & McEwan, M. J. 2007, Icar, 191, 722

Waite, J. H., Young, D. T., Cravens, T. E., et al. 2007, Sci, 316, 870

Wang, D., Gierasch, P. J., Lunine, J. I., & Mousis, O. 2015, Icar, 250, 154

Wells, M., Pel, J.-W., Glasse, A., et al. 2015, PASP, 127, 646

West, R. A., Baines, K. H., Friedson, A. J., et al. 2004, in Jupiter. The Planet, Satellites and Magnetosphere, ed. F. Bagenal, T. E. Dowling, & W. B. McKinnon (Cambridge: Cambridge Univ. Press), 79

Wong, A.-S., Lee, A. Y. T., Yung, Y. L., & Ajello, J. M. 2000, ApJL, 534, L215

Wong, A.-S., Yung, Y. L., & Friedson, A. J. 2003, GeoRL, 30, 1447

Woods, T. N., & Rottman, G. J. 2002, in Atmospheres in the Solar System: Comparative Aeronomy, Geophysical Monograph 130, ed. M. Mendillo, A. Nagy, & J. H. Waite (Washington, DC: American Geophysical Union), 221

Yamamura, I., Tsuji, T., & Tanabé, T. 2010, ApJ, 722, 682

Yelle, R. V., & Miller, S. 2004, in Jupiter. The Planet, Satellites and Magnetosphere, ed. F. Bagenal, T. E. Dowling, & W. B. McKinnon (Cambridge: Cambridge Univ. Press), 185

Yung, Y. L., Allen, M., & Pinto, J. P. 1984, ApJS, 55, 465

Yung, Y. L., & DeMore, W. B. 1999, Photochemistry of Planetary Atmospheres (Oxford: Oxford Univ. Press)

Zahnle, K., Marley, M. S., & Fortney, J. J. 2009, arXiv:0911.0728

Zahnle, K., Marley, M. S., Morley, C. V., & Moses, J. I. 2016, ApJ, 825, 137

Zahnle, K. J., & Marley, M. S. 2014, ApJ, 797, 41

Zurlo, A., Vigan, A., Galicher, R., et al. 2016, A&A, 587, A57